



POLITECNICO
MILANO 1863

**SCUOLA DI INGEGNERIA INDUSTRIALE
E DELL'INFORMAZIONE**

Space Propulsion

Professor: Maggi Filippo
Academic year: 2023-2024



Team Rocket		
Person Code	Surname	Name
10709904	Airoidi	Camilla
10726940	Bachini	Pier Francesco A.
10721571	Belletti	Stefano
10694949	De Luca	Leo
10710062	De Magistris	Matteo
10753159	De Marco	Elena
10987083	Perusini	Gianluca
10113026	Poverini	Viola
10713469	Topuz	Daniele

Submission date: Tuesday 16th April, 2024

Abstract

This report aims at presenting a preliminary study of a new propulsion system, sized to provide an initial nominal thrust of 1 kN and to be operated in vacuum. The system consists in a bi-propellant semi-cryogenic liquid rocket engine with a blow-down architecture. The combustion chamber and the converging part of the nozzle are produced with Selective Laser Melting (SLM) additive manufacturing, using Inconel 718.

At first, a short literature analysis functional to the engine modeling is presented. Then, the thermo-physical parameters are computed and the complete design of the engine is obtained. An evaluation of the thermal analysis is then performed and a check on a regenerative cooling system with RP-1 is done. Lastly, the uncertainties on the design are discussed, focusing in particular on how the production affects the injection orifices dimensions and its consequences on the performances.

Finally, from the analysis of the results, critical observations are made about possible improvements, engine applicability and its overall feasibility.

Contents

1	Literature analysis	1
1.1	Blow-down architecture	1
1.2	Nozzle losses	1
1.3	Metallic additive manufacturing uncertainty	3
1.3.1	Selective Laser Melting (SLM)	3
1.3.2	Surface roughness	4
1.3.3	Accuracy	4
1.3.4	AM in the context of space propulsion	4
1.3.5	Injection plate	5
2	Requirements	6
3	Modeling	6
3.1	Bottom-up	6
3.1.1	Nozzle design	6
3.1.2	Combustion chamber	7
3.1.3	Injection plate design	7
3.1.4	Feeding lines	8
3.1.5	Tank design	8
3.2	Top-down simulation	10
3.3	Thermal analysis	11
3.3.1	Cooling jacket with RP-1	12
3.4	Uncertainty analysis	13
4	Results	14
4.1	Bottom-up sizing	14
4.1.1	Nozzle results	14
4.1.2	Combustion chamber results	15
4.1.3	Injector plate results	16
4.1.4	Tanks results	16
4.2	Top-down simulation results	17
4.3	Cooling sizing results	18
4.4	Uncertainty analysis	19
5	Discussion	23
5.1	Further improvements	23
5.1.1	Injector plate	23
5.1.2	Tanks	23
5.1.3	Thermal analysis	23
5.1.4	Uncertainty analysis	23
5.1.5	Post-machining Refinement	24
5.2	Engine applicability and feasibility	24
6	Conclusion	25
7	Authorship declaration	26

A	Data selection	i
A.1	Reference tables	i
A.2	Selection of L^* , ε_r and ε_c	ii
A.3	Computation of λ and C_d	iii
B	Materials selection and chemical compatibility	iv
B.1	Tanks	iv
B.2	Injection plate and combustion chamber	iv
B.3	Nozzle	iv
B.4	Final selection	v
C	Dittus-Boelter	v

List of Figures

1.3.1 SLM process sketch ^[1]	3
1.3.2 MSFC AM parts ^[2]	4
3.1.1 Feeding lines schematics (dimensions do not represent the actual sizing)	8
3.1.2 Tank layout	9
3.2.1 Top-down flowchart	11
4.1.1 2D engine representation	14
4.1.2 Final configuration: Combustion chamber and convergent - divergent	14
4.2.1 $O/F - c^*$ evolution	17
4.2.2 $I_{sp} - T_{real}$ evolution	17
4.2.3 Mass flow rate and chamber pressure evolution	18
4.4.1 O/F over temperature for the nominal case	19
4.4.2 O/F ratio and \dot{m} evolution	19
4.4.3 I_{sp} evolution	20
4.4.4 P_{cc} evolution	21
4.4.5 Thrust evolution	21
5.1.1 Two different types of tanks	23
A.1.1 Table 5-5 from Sutton book ^[3]	i
A.1.2 Moody diagram ^[4]	i

List of Tables

3.1 Pressure drop induced by each component along the feeding line	8
3.2 Values for thermal analysis	11
4.1 Nominal configuration parameters	14
4.2 Nozzles comparison	14
4.3 Nozzle results	15
4.4 Combustion chamber results	15
4.5 Literature comparison	15
4.6 Injection plate results	16
4.7 Tanks results	16
4.8 Occupied volumes	16
4.9 Thermal analysis results without cooling	18
4.10 Cooling design sizing results	18
4.11 Total impulse $[kNs]$ wrt diameter error	21
A.1 ε_c equal to 12	ii
A.2 ε_c equal to 10	ii
A.3 ε_c equal to 7	ii
B.1 Materials chemical compatibility	iv
B.2 Final materials selection	v
C.1 Values for thermal analysis from Dittus-Boelter model	v
C.2 Thermal analysis results without cooling from Dittus-Boelter model	v
C.3 Cooling design sizing results from Dittus-Boelter model	v

Nomenclature

Symbols

α	Angle for conical divergent nozzle	[deg]
α'	Approximated angle for Rao divergent nozzle	[deg]
β	Angle for convergent part of the nozzle	[deg]
δ_t	Displacement Thickness	[m]
ε_c	Contraction ratio	[–]
ε_r	Expansion ratio	[–]
ε_{In718}	Emissivity of <i>Inconel 718</i>	[–]
η_{bl}	Boundary layers losses	[–]
$\eta_{real,gas}$	Thrust efficiency	[–]
λ	2D losses	[–]
μ	Viscosity	[Pas]
ρ	Density	[kg/m ³]
ρ_{cc}	Mean density in combustion chamber	[kg/m ³]
ρ_t	Density of mixture in throat	[kg/m ³]
ρ_{Ti}	Density of Ti-5Al-2.5Sn	[kg/m ³]
σ	Stefan-Boltzmann constant	[W/(m ² K ⁴)]
σ_{Ti}	Ultimate tensile strength of Ti-5Al-2.5Sn	[Pa]
σ_{In718}	Ultimate tensile strength of <i>Inconel 718</i>	[Pa]
A_{cool}	Surface to be cooled	[m ²]
A_{eff}	Effective area	[m ²]
A_{exit}	Exit area	[m ²]
A_{inj}	Injection area	[m ²]
a_t	Sonic velocity in throat	[m/s]
A_t	Throat area	[m ²]
C_d	Displacement thickness loss	[–]
c_{RP-1}	RP-1 Specific heat	[J/(kgK)]
C_T	Thrust coefficient	[–]
d_c	Characteristic dimension	[m]
D_{cc}	Combustion chamber diameter	[m]
D_t	Throat diameter	[m]
$d_{orifice}$	Injector orifice diameter	[m]
f_{cc}	Friction factor of combustion chamber	[–]
h	Convective heat transfer coefficient	[W/(m ² K)]
I_{sp}	Specific impulse	[s]
$I_{sp,avg}$	Average Specific impulse	[s]

I_{tot}	Total Impulse	[Ns]
k	Specific heat ratio of mixture	[–]
k_{gas}	Thermal conductivity of gas	[W/(mK)]
k_{He}	Specific heat ratio of Helium	[–]
K_{inj}	Head-loss coefficient	[–]
k_{In718}	Thermal conductivity of <i>Inconel 718</i>	[W/(mK)]
L^*	Characteristic length	[m]
L_{cc}	Length of the combustion chamber	[m]
L_{div}	Length of divergent nozzle	[m]
\dot{m}	Mass flow rate	[kg/s]
\dot{m}_{choked}	Choked mass flow rate	[kg/s]
\dot{m}_f	Fuel mass flow rate	[kg/s]
\dot{m}_{ox}	Oxidizer mass flow rate	[kg/s]
\dot{m}_{real}	Real mass flow rate	[kg/s]
\dot{m}_{ideal}	Ideal mass flow rate	[kg/s]
m_{dry}	Dry mass	[kg]
m_{wet}	Wet mass	[kg]
m_{nozzle}	Nozzle mass	[kg]
M	Mach number	[–]
M_{cc}	Mach number in combustion chamber	[–]
Nu	Nusselt number	[–]
$N_{orifice}$	Desired number of orifices	[–]
N	Number of orifices	[–]
O/F	Oxidizer to fuel ratio	[–]
Pr	Prandtl number	[–]
P_{amb}	Ambient pressure	[Pa]
P_{cc}	Nominal combustion chamber pressure	[Pa]
$P_{cc,min}$	Minimum pressure in combustion chamber	[Pa]
$P_{cc,real}$	Pressure at the end of the combustion chamber	[Pa]
P_{exit}	Exit Pressure	[Pa]
P_{tank}	Pressure inside the tank	[Pa]
q_{cond}	Conductive heat flux	[W/m ²]
q_{conv}	Convective heat flux	[W/m ²]
q_{rad}	Radiation heat flux	[W/m ²]
R	Recovery coefficient	[–]
Re	Reynolds number	[–]
Re_{dc}	Reynolds number (characteristic length)	[–]
r_c	Curvature radius	[m]
r_{cc}	Combustion chamber radius	[m]

r_{exit}	Exit radius	[m]
r_t	Throat radius	[m]
th_w	Wall thickness	[m]
th_{cc}	Combustion chamber thickness	[m]
$th_{cc,min}$	Combustion chamber minimum thickness	[m]
th_{tank}	Tank thickness	[m]
t_{res}	Residence time	[s]
T_0	Total temperature	[K]
T_{aw}	Adiabatic wall temperature	[K]
T_{cc}	Combustion chamber temperature	[K]
T_f	Flame temperature	[K]
$T_{fcoolant}$	Final temperature at the end of cooling	[K]
T_{ext}	External ambient temperature	[K]
T_{wh}	Internal wall temperature	[K]
T_{wc}	External wall temperature	[K]
T_{Ideal}	Ideal thrust	[N]
T_{Real}	Real thrust	[N]
v_{cc}	Mean velocity inside combustion chamber	[m/s]
v_{exit}	Exit velocity	[m/s]
v_p	Fluid velocity inside the pipe	[m/s]
V_{conv}	Volume of convergent of nozzle	[m ³]
V_{cc}	Volume of combustion chamber	[m ³]
V_{inj}	Volume of injection plate	[m ³]
$V_{tank,fu}$	Volume of fuel tank	[m ³]
$V_{tank,ox}$	Volume of oxidizer tank	[m ³]
V_{He}	Volume of helium in tank	[m ³]

1 Literature analysis

The literature analysis on blow-down architectures, nozzle losses and uncertainties in metallic additive manufacturing, as presented below, was conducted with the aim of gathering insights to inform the design process of a small rocket engine in accordance with the specifications outlined in Section 3.

1.1 Blow-down architecture

A blow-down system is a type of gas pressure feed in which the propellant and the pressurizing gas (gaseous nitrogen or helium) are stored in the same tank. This inert gas occupies a space above the liquid level of the vessel known as the “ullage”; by letting the ullage expand, the incompressible liquid propellant is pushed into the combustion chamber through the injectors. The flow rate of the liquid propellants diminishes as the differential pressure decreases during their drainage. Consequently, the thrust generated by the rocket motor also diminishes^[5]. In pressurized systems, there are several typical elements designed to provide safety, control, and reusability to the system itself, such as: check valves to prevent propellant backflow, burst diaphragms or isolation valves to isolate the propellants from the pressurizer in order to prevent sloshing, relief valves or relief burst diaphragms to prevent unsafe conditions (for example tank overpressurization) and filters to catch impurities in propellant lines^[3].

When comparing the regulated pressure and the blow-down system, the latter approach results in a simpler, cheaper option, with fewer components with better reliability and lower weight. However, it must be considered that the weight decrease is partly compensated by the rise in propellant due to a lower specific impulse and an increase in tank weight caused by their augmented size and maximum pressure rating. Studies for the *Thor/Delta* and *Atlas/Centaur* class spacecrafts have demonstrated an overall lighter system. A list of advantages and disadvantages is presented below.

Advantages^[3]:

- Simplicity of the system^[6];
- Less gas required^[3];

Disadvantages:

- Thrust decreases as propellant is consumed;
- Higher residual propellant due to less control on the mixture ratio;
- Lower specific impulse toward the end of burning time;
- Larger volume for pressurant as it is stored with the propellant tanks typically at a lower pressure^[6].

The ability of an engine to run stably and predictably over a relatively large inlet pressure range without substantial performance loss determines the viability of this option.

Given its simplicity and low cost, a blow-down architecture is suitable for being mounted on the final stages of a launcher, or directly as the primary thruster of a satellite^[3,7]. Examples of this can be seen in the *Jason2/OSTM* or *Acquarius/SAC-D* propulsion systems.

1.2 Nozzle losses

The ideal nozzle works under a series of assumptions including isentropic quasi-1D, non-reacting, adiabatic flows, neglecting boundary layers or discontinuities^[8]. For real nozzles, dropping these assumptions leads to losses that make some of the internal energy unavailable to be converted into kinetic energy at the exhaust.^[3] The main losses to be considered are listed and described below.

1. Divergence of the flow at the exit section (2D losses)^[3,8]

In an engine, the flow is not perfectly aligned with the axis of the motors because, at the exit of the divergent, the flow in proximity of the wall has a velocity composed of both an axial and a radial component. Since the axial component is the only one that contributes to the thrust, the radial component introduces a loss.

For conical nozzles, losses vary as a function of the cosine of the divergence angle: lower angles lead to small 2D effects, but also to a longer and less compact nozzle. This implies greater frictional losses and inert mass^[9]. To take into account this phenomenon, the divergence loss factor λ was introduced; it can be calculated using Equation (A.3.1) or Equation (A.3.2), depending on the geometry of the divergent part of the nozzle.

These losses can be reduced with a bell-shaped nozzle contour as it is optimized to have the velocity at the exit parallel to the motor axis.

2. Boundary layer effects reduce the average exhaust velocity from 0.5% to 1.5%^[3]

Due to wall friction, real nozzles develop a viscous Boundary Layer (BL) in which the flow is always laminar and subsonic; fluid particles close to the wall have small kinetic energy because of their low velocity. They are therefore stopped by the increase in pressure, and may even be forced to flow in the opposite direction. Under such circumstances, the BL becomes detached from the wall, leading to the development of a recirculation region in close proximity to it^[10].

Another issue caused by the boundary layer is the displacement thickness which is the apparent reduction in the nozzle cross-section and poses a problem for miniaturised systems and low Reynolds numbers. The expression for the divergence coefficient is depicted in Equation (1.2.1), where δ_t denotes the displacement thickness^[11].

$$C_d = \frac{\dot{m}_{real}}{\dot{m}_{ideal}} \approx \frac{A_{effective}}{A_t} \approx \left(\frac{r_t - \delta_t}{r_t} \right)^2 \quad (1.2.1)$$

3. Undesired chemical reactions or chemical reactions within nozzle flows lead to losses of about 0.5%^[3,8]

In the BL region, temperatures might be higher than the ones in the free stream region, due to the conversion of kinetic energy into thermal one that occurs as the velocity is locally slowed down. This phenomenon causes a strong heating effect and an anomalous thermal peak that affects the heat transfer through the walls; this leads to additional chemical reactions in the nozzle that can't take place inside the combustion chamber. Chemical reactions in the nozzle change gas temperature, properties and composition leading to losses.

4. Real gas properties^[3,8]

Real gas properties may modify gas composition leading to losses of about 0.2% to 0.7%.

5. Unsteady combustion and oscillating phenomena are responsible of small losses^[3,8]

Fluctuations in the combustion process affect efficiency and performances.

6. Low nozzle contraction ratios A_1/A_t ^[3,8]

Small chamber or port area ratio cross sections, relative to the throat area or low nozzle contraction ratios, cause pressure losses in the chamber and slightly reduce thrust and exhaust velocity.

7. Transient conditions^[3,8]

Their presence leads to lower performance in terms of pressure inside the combustion chamber, resulting also in a worse behaviour during start, stop and pulsing of the motor.

8. Non-uniform gas composition^[3,8]

A non-uniform composition could lead to incomplete combustion or to a non efficient mixing.

9. Operations at non-optimum design points usually lead to lower performances^[3,8]

No loss is present if the vehicle flies only at the altitude designed for optimum nozzle expansion. In cases in which it operates at lower or higher altitudes, this may cause a loss up to 10% of the thrust and reduce overall performance from 1% to 5%.

Additional loss sources, such as multi phase flow and throat erosion, are not being considered since they primarily affect solid propulsion systems.

1.3 Metallic additive manufacturing uncertainty

The capability of metal Additive Manufacturing (AM) to fabricate complex geometries with significant advantages for lead time and cost, has lead the aerospace industry to be one of its earliest adopters^[12,13]. It is however important to consider that AM is a new technology characterized by some limits including surface roughness, residual stresses, distortion and anisotropy based on the build direction of the component^[13]. These limits bring sources of uncertainty in the processes that result in variability in the quality of the manufactured component^[12].

Each AM process results in different grain structures, which ultimately influence properties of the manufactured part^[13]. Out of the seven classes of AM technology categorized by the ISO/ASTM 52900, the most adapt for metallic AM are Direct Energy Deposition (DED) and Power Bed Fusion (PBF); these are further defined as a function of the primary heat source, such as laser (L) or electron beam (EB)^[14,15]. This selection is supported by the their extensive industrial adoption to fabricate metal components^[12].

In particular, laser powder bed fusion (L-PBF), also known as selective laser melting (SLM), has become the most widely used process for AM of complex parts in aerospace, due to its high resolution and high-quality part production capabilities, combining fine feature sizes with adequate build volumes^[16,17]. Additional advantages such as high-flexibility of metallic feed-stock powders and a better surface finish than DED, make this process and its uncertainties the main focus of this literature analysis^[1]. Other process categories are not discussed as they are still in evolution with a lower TRL^[12,16].

1.3.1 Selective Laser Melting (SLM)

To understand the additive manufacturing uncertainties, it is important to understand the production process. For the SLM process, a powder bed is selectively hit by a high-powered laser beam that causes its particles to fuse together. A scanning mechanism adjusts the laser's focal point to match the outline of the intended component. After this procedure, the build platform lowers, and a new powder layer is applied with a recoater system. This new layer is selectively exposed to the laser repeating the process until the complete height of the part is obtained. The operation occurs within an argon-filled chamber to prevent contamination from oxygen and nitrogen, ensuring the integrity of the processed metal^[1,18].

An overview of these components is shown in Figure 1.3.1.

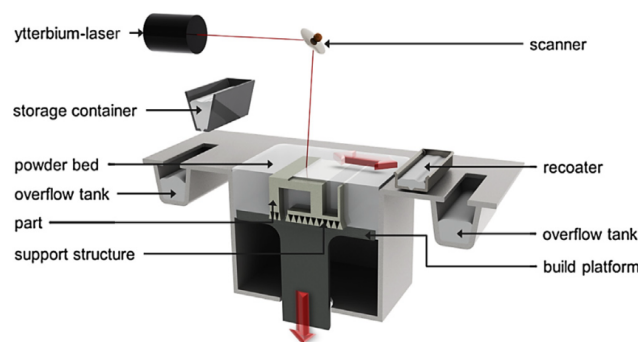


Figure 1.3.1: SLM process sketch^[1]

Commonly used SLM powder materials are Ni-based superalloys, Fe-alloys and Ti-alloys. Inconel 718/IN718 is the most used Ni-based superalloy in aerospace industry due to its superior mechanical properties at elevated temperatures: it has the capability of withstanding stresses up to an operating temperature close to 704°C ^[19], a high phase stability thanks to face-centred-cubic (FCC) nickel matrix, and the capability to be strengthened by other alloys such as chromium and/or aluminium. Fatigue and fracture properties, as well as resistance to corrosion and oxidation are other features that make this material the best choice for additive manufacturing^[1,20].

1.3.2 Surface roughness

The advantages of AM were previously mentioned; however, poor surface quality and surface topography imperfections are inherent in metal AM and are among the main drawbacks of this method^[21]. In SLM, this high surface roughness is caused by partially melted powders and/or pores on the outer surface^[17]. This has also been confirmed for Inconel 718 components, since studies have shown that, with this material, SLM successfully obtains comparable mechanical properties, fatigue, and creep resistance with respect to traditional manufacturing methods, whilst the surface quality is not at the same level^[17]. Available literature on the values for the roughness of Inconel 718 with SLM shows contrasting results, with ranges of $5 - 10\ \mu\text{m}$ or $> 20\ \mu\text{m}$ ^[17,22,23,24]. For the design process, the most conservative value of $21\ \mu\text{m}$ shall be used.^[22]

1.3.3 Accuracy

The accuracy of the final product produced with AM is influenced by several factors that need to be taken into consideration to provide high dimensional and shape precision. These factors include laser parameters, powder characteristics, material properties of powder and printing chamber environment.^[25]

Additional sources of uncertainties need to be avoided by positioning correctly the model in the machine's workspace, since an incorrect choice can lead to sudden changes of consequent cuts, resulting in high internal tension.^[18] The temperature of the base plate is also important to prevent deformations during cooling due to the internal tension. Setting it to a high temperature ($\sim 200^{\circ}\text{C}$) has been shown to be a solution for this; however it is important to stay below the threshold of the recommended temperature for annealing.^[18] High-resolution SLM is able to build at a layer thickness of $0.02\ \text{mm}$, and can produce parts with tolerances of $\pm 0.76\ \text{mm}$ and part features as small as $0.152\ \text{mm}$.

1.3.4 AM in the context of space propulsion

The NASA Marshall Space Flight Center (MSFC) is taken as a case study to show the use of metal AM for space propulsion components and its challenges. Between 2012 and 2018, MSFC has fabricated over 10 unique AM chambers and injectors with SLM using Inconel 625, Inconel 718, Monel K-500 and other materials. As expected, they found challenges in the feature size resolution (particularly radial to the build direction), and excessive surface roughness of the injectors. Using SLM, the minimum hole size they could produce was of $0.4\ \text{mm}$ ^[23]. Examples of finished assemblies from this group are shown in Figure 1.3.2:



Figure 1.3.2: MSFC AM parts^[2]

1.3.5 Injection plate

Since the injection plate design is later carried out using a procedure not seen in class, a brief literature analysis was performed.

To maximize the advantages of AM for the injector plate design, the orifice sizing can be computed with a method that uses the head-loss coefficient instead of the more common flow coefficient. This is because the head loss coefficient (K) permits to calibrate different specs of the orifice, which exploits the flexibility of the hole sizing in SLM^[26]. The head loss coefficient is the sum of entrance-loss coefficient, running friction loss and the exit loss one.

Using this model, the desired number of orifices in the plate becomes a variable which can be chosen arbitrarily. For maximum atomization a high value for it should be chosen, keeping in mind the limits of the production technology adopted. As a matter of fact, one of the limits is found in the realisation of the angles of the orifices which are limited by the AM technique where the maximum achievable angles are 45° in order to have an impinging effect and structural stability^[27].

2 Requirements

The following report aims to design and complete a performance evaluation for a new liquid semi-cryogenic rocket engine (LOX-RP1) to be operated in a vacuum, based on the given requirements:

- The initial thrust shall be of 1 kN;
- The initial chamber pressure shall be of 50 bar, with a minimum of 20 bar;
- The system shall be allocated in a cylinder of 2 meter length and 1 meter diameter; the available space for tanks, combustion chamber and convergent part of the nozzle is to be considered the 80% of the volume;
- The architecture of the system shall be a blow-down one;
- The injection plate and the combustion chamber shall be produced using additive manufacturing.

3 Modeling

The modelling is carried out dividing the whole procedure into two different parts: the *Bottom-Up* and the *Top-Down*. The first one is used to find the initial configuration and the system geometries to respect the given constraints; then, in the second analysis, the outputs of the bottom-up are used as input parameters to simulate the entire behaviour of the engine over time.

During the modeling, the Chemical Equilibrium Applications (CEA) is used to compute some thermodynamic properties of the flow, setting as inputs chemical species, the O/F ratio and the pressure in the combustion chamber P_{cc} .

3.1 Bottom-up

The bottom-up analysis starts from the nozzle design and proceeds backwards finishing with the tank sizing.

3.1.1 Nozzle design

To meet the design requirement of $T_{nominal} = 1kN$ whilst accounting for the nozzle and combustion chamber losses, an iterative approach was implemented.

After assuming an isentropic, quasi 1-D nozzle flow, an expansion ratio of $\varepsilon_r = 200$ was selected from the nominal range of 100-400 for in-space application.^[26] This value was a trade off between specific impulse and nozzle length, whose evaluation can be found in Appendix A.2. This allowed to numerically solve Equation (3.1.1) and recover the exit pressure P_{exit} of the divergent nozzle, where $P_{cc,real}$ is the pressure at the end of the combustion chamber considering a pressure drop from the nominal P_{cc} as explained in Section 3.1.2. For the first iteration $P_{cc,real}$ was set to be equal to P_{cc} (50bar) and T_{ideal} was set to 1 kN.

$$\frac{1}{\varepsilon_r} = \left(\frac{k+1}{2} \right)^{\frac{1}{k-1}} \left(\frac{P_{exit}}{P_{cc,real}} \right)^{\frac{1}{k}} \sqrt{\frac{k+1}{k-1} \left[1 - \left(\frac{P_{exit}}{P_{cc,real}} \right)^{\frac{k-1}{k}} \right]} \quad (3.1.1)$$

Once P_{exit} was derived, it was possible to calculate C_T with Equation (3.1.2). The throat area was then computed by inverting the definition of C_T , through Equation (3.1.3). P_{amb} is here assumed to be 1Pa, as for medium vacuum^[28].

$$C_T = \sqrt{\frac{2k^2}{k-1} \left(\frac{2}{k+1} \right)^{\frac{k+1}{k-1}} \left[1 - \left(\frac{P_{exit}}{P_{cc,real}} \right)^{\frac{k-1}{k}} \right]} + \frac{P_{exit} - P_{amb}}{P_{cc,real}} \varepsilon_r \quad (3.1.2) \quad A_t = \frac{T_{ideal}}{P_{cc,real} \cdot C_T} \quad (3.1.3)$$

The throat area is connected to the combustion chamber area through the contraction ratio ε_c , which was selected between 5-15 in order to obtain a reasonable combustion chamber geometry compliant with the

necessity of designing an injection plate. The selection procedure can be found in Appendix A.2. Fixing this value at 10, both the convergent and the divergent nozzle areas were defined. This allowed to compute the losses described in Section 1.2 that depend on the exit conditions derived at each iteration.

The real thrust was calculated as:

$$T_{real} = \eta_{real,gas} \cdot (\lambda \cdot \eta_{bl} \cdot C_d(\dot{m} \cdot v_{exit}) + A_{exit}(P_{exit} - P_{amb})) \quad (3.1.4)$$

Where $\eta_{real,gas}$ and η_{bl} were assumed respectively equal to 0.7 and 1.5 as conservative values taken from the literature analysis in Section 1.2. λ and C_d were evaluated at each time step as explained in Section 1.2.

The cycle was repeated incrementing at each step T_{ideal} so to obtain a geometry able to guarantee $T_{real} = 1kN$ as the effective thrust generated.

3.1.2 Combustion chamber

The diameter of the combustion chamber was fixed from the modeling of the convergent nozzle. To obtain the total volume, a L^* was selected^[26]. The chosen value of 50" (1.27 m) leads to a longer chamber to better respect the assumption of frozen expansion model in the nozzle.

A pressure drop in the combustion chamber was considered through the Darcy-Weisback Equation^[29] shown in Equation (3.1.5), to take into account the surface roughness due to the AM. The friction factor was obtained from the Moody diagram, assuming a constant Reynolds during time^[3] and a value of 21 μm for the roughness as shown in Section 1.3.2. The ρ_{cc} is the mean density in the combustion chamber computed from CEA.

$$\frac{\Delta P}{L_{cc}} = f_{cc} \frac{\rho_{cc}}{D_{cc}} \frac{v_{cc}^2}{2} \quad (3.1.5)$$

To define the thickness of the combustion chamber, a minimum manufacturing value together with a minimum to guarantee the structural strength was considered. The structural limit was imposed through Equation (3.1.6), with a sizing pressure equal to the maximum 50 bar applying a safety factor of 2.

$$th_{cc,min} = 2 \frac{P_{cc} r_{cc}}{\sigma_{In718}^{[30]}} \quad (3.1.6)$$

3.1.3 Injection plate design

Among the possible architectures for the design of the injection plate, a *like on like* configuration was selected.^[3,31] Despite less mixing performance, the simplicity of manifold and the better safety against failure justify this choice. For the arrangement of the holes a configuration made by concentric rings with alternating bands of fuel and oxidizer was chosen, following the same arrangement of the F1 engine injector plate^[31].

The injection area was sized using Equation (3.1.7) in order to guarantee the O/F ratio at 50 bar. A starting pressure drop at injection equal to 20% of the initial chamber pressure was considered^[26]. This pressure drop will vary with the square of velocities during draining, as shown in Section 3.2.

A head-loss coefficient (K_{inj}) of 1.7 was chosen: this corresponds to a sharp edge orifice and it is a sum of entrance loss coefficient 0.5, a running friction loss 0.2, and an exit loss taken from literature as a theoretical value of 1.^[26]

$$A_{inj} = \dot{m} \sqrt{\frac{2.238 K_{inj}}{\rho \Delta P}} \quad (3.1.7)$$

The diameter of the orifices is computed for both the fuel and the oxidizer. This is done through an iterative process that consists in starting from $N = 2$ and increasing it until the diameter reaches the minimum set value of 0.5 mm. This was obtained in correspondence to the literature analysis, starting from the minimum possible hole diameter of 0.4 mm and adding the uncertainty and the roughness caused by AM. At each iteration, the diameter is computed using Equation (3.1.8).

$$d_{orifice} = \left(\frac{3.627 K_{inj} \dot{m}^2}{\rho \Delta P N^2} \right)^{0.25} \quad (3.1.8)$$

If the N found for the minimum allowable diameter was odd, because of the *like on like* constraint, $N - 1$ is taken.

Furthermore, given the like on like selection, the impinging angles can be chosen in the allowed technological range given by the AM (Section 1.3.5).

3.1.4 Feeding lines

The feeding system is composed of two different lines, one for the oxidizer and one for the fuel. A diameter of 5 mm for both lines was assumed, aligned with typical literature values^[32]. To model it, both localized and distributed pressure losses were considered.

The effect of the concentrated losses was designed considering the pressure drop induced by one control valve, one latch valve and one filter per line. Their respective values were taken from the producer's datasheet. Since the length of the feeding line was not modeled, an average value of 50 kPa was selected to take into account the distributed losses. These values are summarized in Table 3.1.

Component	Pressure loss [bar]
Fill and Drain valve	1.0342 ^[33]
Filter	0.756 ^[33]
Latch valve	1.0342 ^[34]
Distributed loss	0.5

Table 3.1: Pressure drop induced by each component along the feeding line

In Figure 3.1.1 the scheme of the feeding lines is represented.

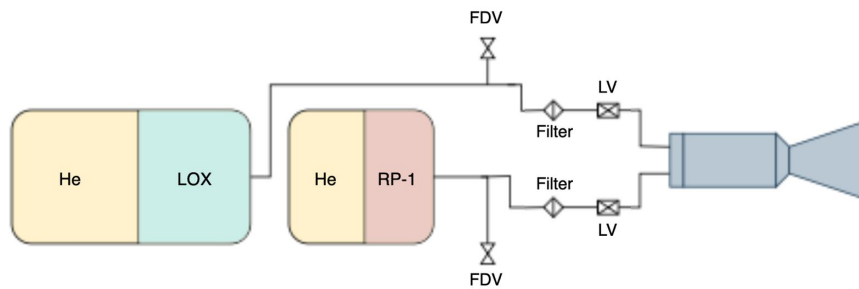


Figure 3.1.1: Feeding lines schematics (dimensions do not represent the actual sizing)

3.1.5 Tank design

The tanks were designed in order to guarantee the desired pressure at injection of 50 bar at the start of the simulation. To maximise performances, the amount of propellant stored and tank volumes was computed to fully occupy the available space left out from the other components of the initial 80% of the total volume (the starting total available volume is computed at this point and it is fixed). The relative volumes of the fuel and oxidizer were chosen to match an initial mass O/F ratio of 2.24, which is then used to compute the volumetric O/F ratio of 1.57^[3].

In the evaluation of the required pressure inside each tank, an additional loss was taken into account on top of the ones described in the feeding lines and the injection plate modeling. This consisted in the dynamic

pressure drop as the fluid exits the tank, computed as $\Delta P_{dyn} = \frac{1}{2}\rho v_p^2$, where v_p is the velocity in the pipe, which is different for the oxidizer and fuel line.

To compute the velocity at the initial and final states, the pipe diameter and the mass flow rate in each line were used. The O/F ratio and the mass flow rate obtained from the nozzle design were used to compute the initial and final mass flow rates for the two lines. In this case, the O/F ratio was considered constant, since at this point of the design its evolution over time was not known.

Thus, the required initial pressure for both tanks was evaluated as:

$$P_{tank} = P_{cc} + \Delta P_{feed} + \Delta P_{inj} + \Delta P_{dyn} \quad (3.1.9)$$

The chosen material for the tanks was a Titanium alloy, Ti-5Al-2.5Sn, characterized by strain $\sigma_{Ti} = 861 \text{ MPa}$ and a density $\rho_{Ti} = 4480 \text{ kg/m}^3$ ^[35]. The oxidizer tank was internally coated with a layer of steel SS304L, in order to avoid triggering any violent chemical reaction due to the interaction between Titanium and liquid oxygen (see Appendix B).

Following this considerations, a computation was set to find the volumes and dimensions of the two tanks, where the following constraints were imposed:

1. Both the initial and final volumes of the helium and its pressure evolution must satisfy an adiabatic transformation (1st and 2nd equations). This assumption holds true since the time scale of the draining is short with respect to the time taken for the rebalancing of temperatures; otherwise, an isothermic expansion should be accounted.
2. The helium final volume must be equal to the total tanks volume minus the volume occupied by the thickness of the tanks.
3. The initial O/F ratio must be respected at all times (4th equation).
4. A margin of 2%^[36] of the initial stored mass was applied to account for oxidiser/fuel residuals, so that the tanks are not fully empty once the chamber reaches a pressure of 20 bar.
5. The total volumes balances are imposed with formulas 5 to 8 (and 3).

The procedure to compute the volume of the tanks was the following: First of all, the external diameter of each tank was selected to be equal to 1 m, the maximum one available from constraint. This way it was possible to size the thickness of the tank through Equation (3.1.6) with a safety factor of two over the maximum pressure. Then, an iterative cycle was started to compute the final volumes with Equation (3.1.10), each step reducing the initial guessed diameter of the fuel tank (to match the desired free space on the sides) and recalculating the thickness until all constraints were respected.

A schematic depiction of the resulting tank layout following this procedure is shown in Figure 3.1.2, where V_2 and V_4 refer to the tank volumes without the thickness.

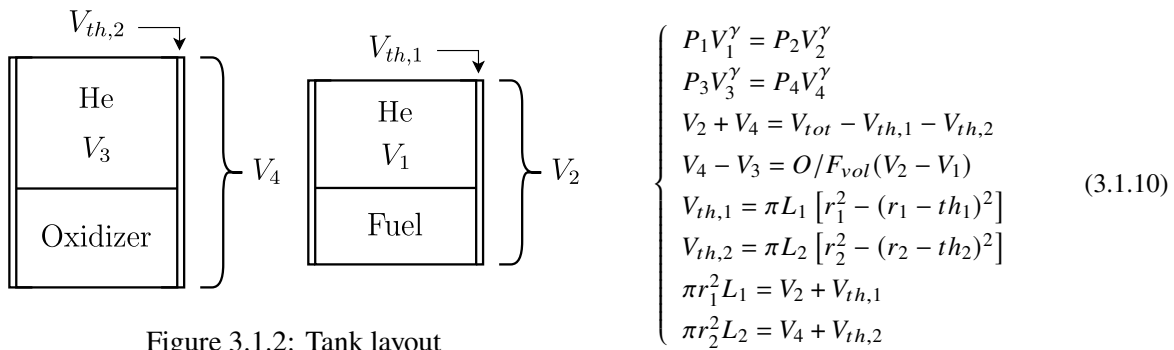


Figure 3.1.2: Tank layout

After computing the volumes, a consideration on the positioning of the tanks was made. The fuel tank was placed in between the oxidizer tank and the combustion chamber to reduce problems related to different storing

temperatures, which correspond to 294.4K for RP1 and 90.37K for LOX. The fuel tank was also centered in the remaining free space to have a better weight distribution and leaving room for the feeding lines which were not modeled.

The final masses were found by multiplying the resulting volumes for their respective densities interpolated from the NIST webbook^[37]. In the computations, the portion of the internal tank volume occupied by the membrane and tubing was neglected.

3.2 Top-down simulation

Once all the subsystems were designed in Section 3.1 to match the requirements, it was possible to simulate the development of performances over time starting from the fixed initial condition until the condition of $P_{cc,min}$.

Both the pressure losses for the fuel and the oxidizer described in the previous section can be compactly written in the form:

$$P_{tank} = \alpha v^2 + \beta + P_{cc} \quad (3.2.1)$$

Where α is a function of the density of the flow and the diameter of the injector holes, and β depends on the concentrated and distributed losses in the feeding lines.

In the hypothesis of having a P_{cc} , and knowing the initial helium (and thus fuel/oxidizer) pressure, the velocity in both pipes can be computed by inverting Equation (3.2.1).

Having the velocity in the pipes, the mass flow rates \dot{m}_f and \dot{m}_{ox} are trivially computed using the pipe area and oxidizer/fuel density; this also gives the O/F ratio.

Given a certain chamber pressure, the mass flow rate is uniquely identified for a choked nozzle. It can be easily computed using the sonic velocity a_t and combustion gas density ρ_t at throat, that are outputs of the CEA with the chamber pressure and the previously computed O/F ratio as inputs.

$$\dot{m}_{choked} = \rho_t A_t a_t \quad (3.2.2)$$

Given this, to find the P_{cc} providing a total mass flow from the tanks that is equal to the choked mass flow computed above, the equation $\dot{m}_{choked} = \dot{m}_f + \dot{m}_{ox}$ was solved. For this purpose, a bisection method was employed in spite of a linear search, for better precision and less computational time. With the computed chamber pressure the oxidizer/fuel pipe velocities, and thus mass flow rates, can be computed from Equation (3.2.1).

Given the time iteration step Δt , the mass flowing out of the tanks during a single time step is $\dot{m}\Delta t$. Dividing this value by the oxidizer and fuel densities the corresponding volumes can be computed. Logically, a flow of oxidizer/fuel out of the tanks corresponds to an equal volume increase in the pressurant, and with such volume the new tank pressure can be computed assuming an adiabatic transformation as:

$$P_{tank}^{new} = P_{tank}^i \left(\frac{V_{He}^i}{V_{He}^{new}} \right)^{k_{He}} \quad (3.2.3)$$

With the new tank pressure the simulation was able to advance to the next time step, and stopped once the minimum chamber pressure was reached. At each time step, the specific impulse I_{sp} was obtained from CEA and, combined with the previously computed mass flow rate, the thrust could be calculated.

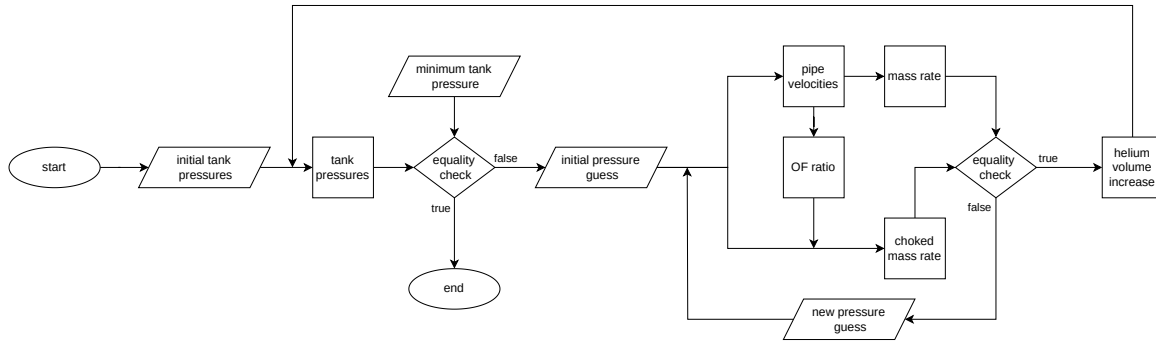


Figure 3.2.1: Top-down flowchart

3.3 Thermal analysis

In order to study the behaviour of the combustion chamber and the convergent part of the nozzle during the firing, a thermal analysis was performed. The heat transfer mechanism chosen to compute the values considers the following approximations:

- conservation of heat flux thorough the whole process (steady state);
- heat transfer inside the combustion chamber and nozzle only by convection and conduction;
- uniform radiative heat exchange with outer space.

The CEA was used for the computation of the dynamic viscosity coefficient (μ), the thermal conductivity of the gas (k_{gas}), the Reynolds (Re) and Prandtl (Pr) numbers in both the combustion chamber and the throat. The correlation for the Nusselt (Nu) number is chosen between the formulation of Gnielinski and Dittus-Boelter. Considering the CEA results and the validity range for both formulations, the Gnielinski approach was applied with Equation (3.3.1). A Dittus-Boelter analysis was still conducted, with results shown in the Appendix C.

$$Nu = \frac{h d_c}{k_{gas}} = \frac{(f_{cc}/8)(Re - 1000)Pr}{1 + 12.7(f_{cc}/8)^{1/2}(Pr^{2/3} - 1)} \begin{cases} 0.5 \leq Pr \leq 2000 \\ 3000 \leq Re_{dc} \leq 5 \cdot 10^6 \end{cases} \quad (3.3.1)$$

	Re_{dc} [-]	Pr [-]	h [W/(m²K)]
Combustion chamber	6.77e+04	0.620	1.32e+03
Throat	2.23e+05	0.625	1.28e+04

Table 3.2: Values for thermal analysis

The characteristic length (d_c) is equal to the hydraulic diameter (D_{cc}) of the combustion chamber, for the throat it is equal to its diameter (D_t).

By inverting Equation (3.3.1), the coefficient h of the gas was obtained, for the case of the convergent, h was computed at the throat, being the most critical condition. This value was then used to apply the *Newton's law of cooling* to obtain the heat flux from the combustion chamber to its walls, the same reasoning was applied for the nozzle's throat.^[38]

T_{aw} was computed expliciting the recovery coefficient, the total temperature, and the Mach number in the combustion chamber.

$$q_{conv} = h(T_f - T_{wh}) \quad (3.3.2)$$

To find the heat flux through the walls, the approximation of conductive transfer was adopted resulting in:

$$q_{Cond} = -k_{In718} \frac{T_{wh} - T_{wc}}{th_w} \quad (3.3.3)$$

Where k_{In718} of *Inconel 718* was obtained from the datasheet^[19].

Considering the ambient temperature T_{ext} at 2.7K, and approximating the behaviour of the wall to a Grey body, Equation (3.3.4) was used to compute the heat flow from the external wall to the ambient.^{[39][38]}

$$q_{Rad} = \sigma \varepsilon_{In718} (T_{wc}^4 - T_{ext}^4) \quad (3.3.4)$$

where ε_{In718} is the emissivity of *Inconel 718*^[40].

Following the steps below, an iterative process was used to find the correct internal and external temperatures of the wall, which guarantees continuity of the heat flow.

1. Hypothesise the internal wall temperature T_{wh} ;
2. Compute q_{conv} from Equation (3.3.2) using the starting hypothesis on T_{wh} ;
3. Obtain T_{wc} by inverting Equation (3.3.3) and imposing conservation of heat flux;
4. Compute Equation (3.3.4) using the calculated T_{wc} ;
5. Verify that $q_{cond} \approx q_{Rad}$; if not, repeat the loop.

3.3.1 Cooling jacket with RP-1

The possibility of cooling down the combustion chamber and the convergent part of the nozzle using RP-1 was evaluated.

The following analysis starts from a desired wall temperature that guarantees the nominal mechanical properties, moreover verifies if the liquid fuel stored in the tank is sufficient to cool down the system without reaching the coking temperature.

First, the total power exchanged from the flame to the wall was computed from Equation (3.3.5) using the h computed with Equation (3.3.1):

$$\begin{cases} q_{conv} = h (T_{aw} - T_{ac}) \\ T_{aw} = \frac{1+Pr^{1/3} \frac{\gamma-1}{2} M^2}{1+\frac{\gamma-1}{2} M^2} T_0 \end{cases} \quad (3.3.5)$$

The temperature variation of the fuel that grants the correct cooling is computed from Equation (3.3.6)

$$\Delta T = \frac{q_{conv} A_{cool}}{\dot{m}_f c_{RP-1}} \quad (3.3.6)$$

In Equation (3.3.6), A_{cool} is the lateral surface that differs between combustion chamber and convergent. Since the mass flow rate of the propellant varies during the firing, a mean value (\dot{m}_f) was used in the formula. The computed temperature variation was compared to the coking temperature. Then the needed fuel mass to cool the combustion chamber was compared with the available one.

3.4 Uncertainty analysis

Given the selection of the SLM additive manufacturing process with Inconel 718, a level of uncertainty is to be expected; this can have a significant impact on smaller features, such as the holes in the injection plate.

Following the literature analysis, a maximum tolerance of $\pm 76 \mu m$ and a roughness of $21 \mu m$ was considered for the investigation. The tolerance was applied in both directions of the diameter, whilst the roughness contribution was taken as a narrowing effect. The total error is taken as the sum of the two.

The uncertainty analysis was performed by running the top-down simulation, with four different extreme combinations that present the most variable cases for the mass flow rate and the OF ratio:

- Both oxidizer and fuel injector diameters with the maximum enlarging error;
- Both oxidizer and fuel injector diameters with the maximum narrowing error;
- Oxidizer injector diameters with the maximum enlarging error, and fuel injector diameters with the maximum narrowing error;
- Fuel injector diameters with the maximum enlarging error, and oxidizer injector diameters with the maximum narrowing error.

The results obtained were then compared to the nominal case.

4 Results

In the following section the results and performances of the sizing are described for each subsystem. In Table 4.1 the main engine performances are summarized in the nominal configuration, that is without considering the uncertainties on the injection holes.

$I_{sp,avg} [s]$	$I_{tot} [MN \cdot s]$	$t_{burn} [min]$	$m_{dry} [kg]$	$m_{wet} [kg]$
359.68	1.7391	48.0833	172.4472	714.1852

Table 4.1: Nominal configuration parameters

4.1 Bottom-up sizing

In Figure 4.1.1 the complete assembly is shown with the resulting geometries.

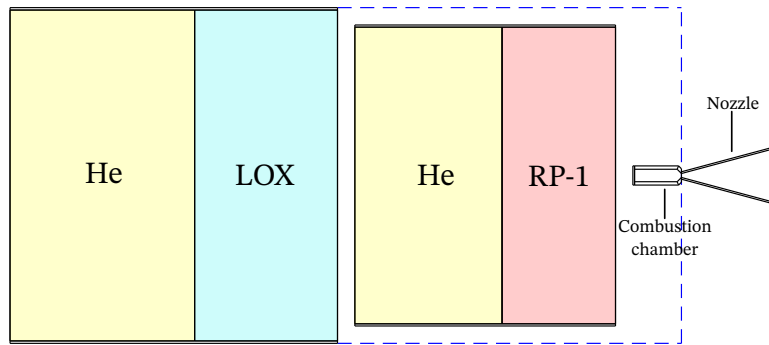


Figure 4.1.1: 2D engine representation

4.1.1 Nozzle results

Two possible geometries of divergent nozzle were taken into account. The first one is a bell nozzle and it is obtained via Rao approximation with the same length as the reference one. The second one was imposed to have the same length of the Rao nozzle, but with a 15 degrees conical shape. In Table 4.2, a comparison between the two is shown, comparing performance and mass. The selected material was graphite; a better explanation of this choice can be found in Appendix B.

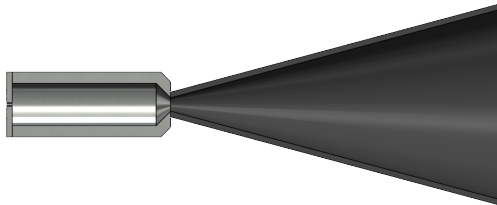


Figure 4.1.2: Final configuration: Combustion chamber and convergent - divergent

	T_{real}/T_{ideal}	$m_{nozzle} [kg]$
Bell nozzle	0.965	1.95
Conical nozzle	0.956	0.79

Table 4.2: Nozzles comparison

Since the approximated bell nozzle resulted in a slight increase of performances at the cost of higher weight and manufacturing complexity, the conical one was chosen.

The geometries of convergent and divergent nozzles are summarized in Table 4.3, where the convergent geometry was obtained by fixing β at 45° .

$r_{cc} [cm]$	$r_t [cm]$	$r_{exit} [cm]$	$L_{con} [cm]$	$L_{div} [cm]$
1.86	0.59	8.30	1.27	28.78

Table 4.3: Nozzle results

4.1.2 Combustion chamber results

The design of the combustion chamber yields the following results:

$L_{cc} [cm]$	$A_{cc} [cm^2]$	$V_{cc} [cm^3]$	$th_{cc} [cm]$	$M_{cc} [-]$	$\Delta P_{cc} [Pa]$	$t_{res} [ms]$
12.7	11	137.4	1	0.0597	743.2	1.7

Table 4.4: Combustion chamber results

The resulting geometry is a trade off between reducing the losses inside the combustion chamber and increasing the residence time for fuel and oxidizer to react. The pressure losses due to the superficial roughness obtained with additive manufacturing represent a minor influence overall.

The resulting geometry leads to a low Mach number inside the chamber and a velocity in the order of 76 m/s. This can be considered a reasonable result, since the length of the combustion chamber guarantees a residence time of about 1.7 ms. Those results were compared with three cases found in literature that have similar geometry and thrust, but different propellant couples with respect to the designed ones. The comparison supported the value of the Mach number in the chamber and, as a consequence, the residence time of the mixture. The Mach number and the t_{res} in Table 4.5 were reverse-engineered from the available data in the literature.

	$T [N]$	$L_{cc} [cm]$	$A_{cc} [cm^2]$	$T_{cc} [K]$	$M_{cc} [-]$	$t_{res} [ms]$
GOX/Ethanol ^[41]	2758	10.16	14.70	1200	0.006	23.5
GOX/Ethanol-water mixture ^[42]	1000	9.05	44.18	3030	1.021e-04	789.5
N₂O₄/MMH ^[43]	450	8.50	6.16	3385	1.5279e-04	446.5

Table 4.5: Literature comparison

From the computation, the minimum thickness to guarantee structural strength, without considering the operating temperature, was in the order of 0.2 mm, compliant with the limits of additive manufacturing. Nevertheless, the chosen value was 1 cm to account for the necessity of having cooling channels inside the combustion chamber wall and a wall temperature that grants the correct mechanical properties. The same thickness has been chosen for the convergent nozzle.

4.1.3 Injector plate results

The results of the process described in Section 3.1.3 are displayed in the following table:

	$A_{inj} [mm^2]$	$d_{inj} [mm]$	N_{inj}	$th_{inj} [cm]$
RP-1	3.05	0.527	14	0.5
LOX	5.72	0.509	28	0.5

Table 4.6: Injection plate results

Thanks to the AM process it is possible to obtain diameters for the propellants that are not standard, but weighted to the necessity imposed: having the highest number of orifices in order to have a better atomization and mixing, while remaining above the minimum diameter achievable by AM considering also its tolerances, in this case set at $0.5mm$; the iterative process described in Section 3.1.3 managed to fulfill the desired values. With the resulting design the plate is to be manufactured using AM and the same material adopted for the combustion chamber.

To set the thickness of the injector plate, a reasoning similar to the one described in Section 4.1.2.

4.1.4 Tanks results

In Table 4.7 the tanks geometry and mass of initially stored oxidizer/fuel are reported.

	$m [kg]$	$m_{tank} [kg]$	$L_{tank} [m]$	$r_{tank} [m]$	$th_{tank} [mm]$	$m_{he} [kg]$	$P_{tank} [bar]$
RP-1	167.20	63.35	0.78	0.45	6.5	2.71	63.48
LOX	374.53	99.56	0.98	0.50	7.3	4.25	63.83

Table 4.7: Tanks results

It can be noticed that the choice of Ti-5Al-2.5Sn, given its high ultimate strength, allowed to obtain a low thickness and low weight considering the amount of stored propellant and the dimension of the tanks. In fact, if the whole sizing would have been carried out with SS304 instead of Ti-5Al-2.5Sn, the resulting total mass of both tanks would have been 408 kg. For this reason the Ti-5Al-2.5Sn was chosen, even with the cons of needing an internal coat in SS304^[44] in the oxidizer tank, for compatibility.

After the tank sizing, the requirement of 20% free space can be verified by checking the occupied volume fraction of the components, as can be seen in Table 4.8.

$V_{tank, fu} [m^3]$	$V_{tank, ox} [m^3]$	$V_{cc} [cm^3]$	$V_{inj} [cm^3]$	$V_{conv} [cm^3]$	$V_{tot} [m^3]$	$V_{occupied} / V_{tot}$
0.49	0.77	3.36	0.13	0.16	1.57	0.8

Table 4.8: Occupied volumes

4.2 Top-down simulation results

With the methodology previously explained, all the engine performance parameters history can be computed. The simulation time step was chosen as $\Delta t = 5$ s, as lowering it further only increased computational time without noticeable changes to the outputs.

As shown in Figure 4.2.1a, during engine operation, the value of the O/F ratio remains approximately constant, thus verifying the bottom-up sizing of the tanks, that had such assumption. The c^* is also expected to have little variations, as verified by the simulation.

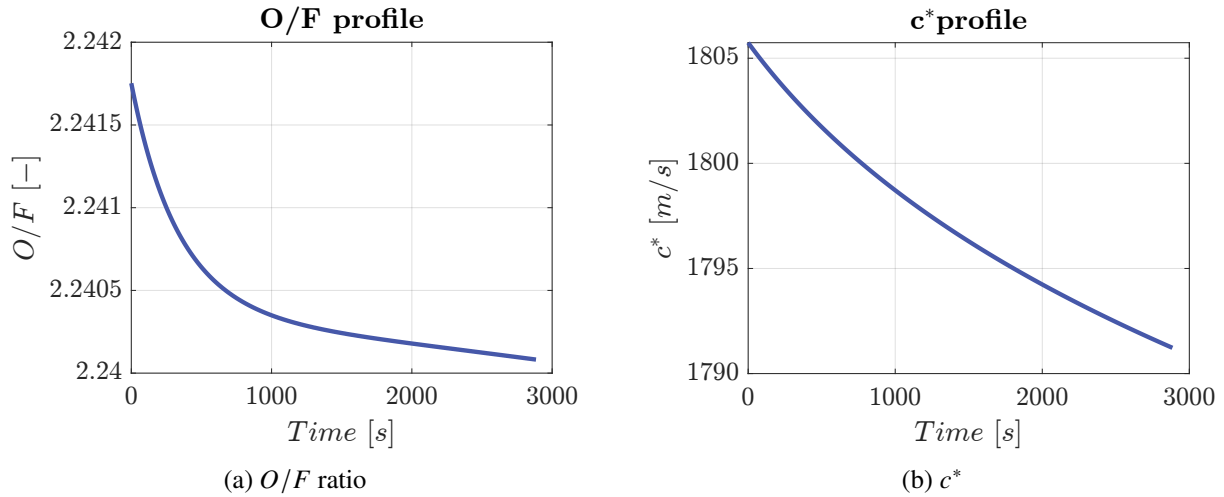


Figure 4.2.1: $O/F - c^*$ evolution

In Figure 4.2.2a, the I_{sp} also stays approximately constant, while the thrust starts at the initial design requirement of 1kN, and then keeps decreasing until reaching a final value of around 400N. This decrease is expected, as during operation the mass flow rates also keeps decreasing along with the pressure inside the tanks due to the blow-down architecture. This can be observed in Figure 4.2.3b. Because of the decreasing pressure of the helium, the rate of change of the thrust decreases with time.

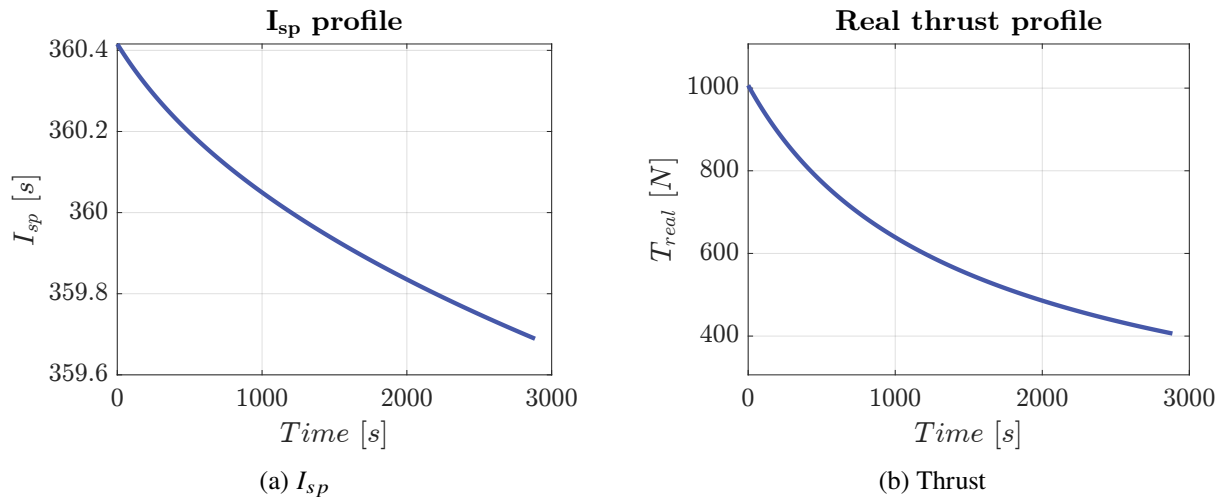


Figure 4.2.2: $I_{sp} - T_{real}$ evolution

In Figure 4.2.3a, it can be appreciated that the mass flow rate has the same profile as the thrust, as the I_{sp} remains essentially constant.

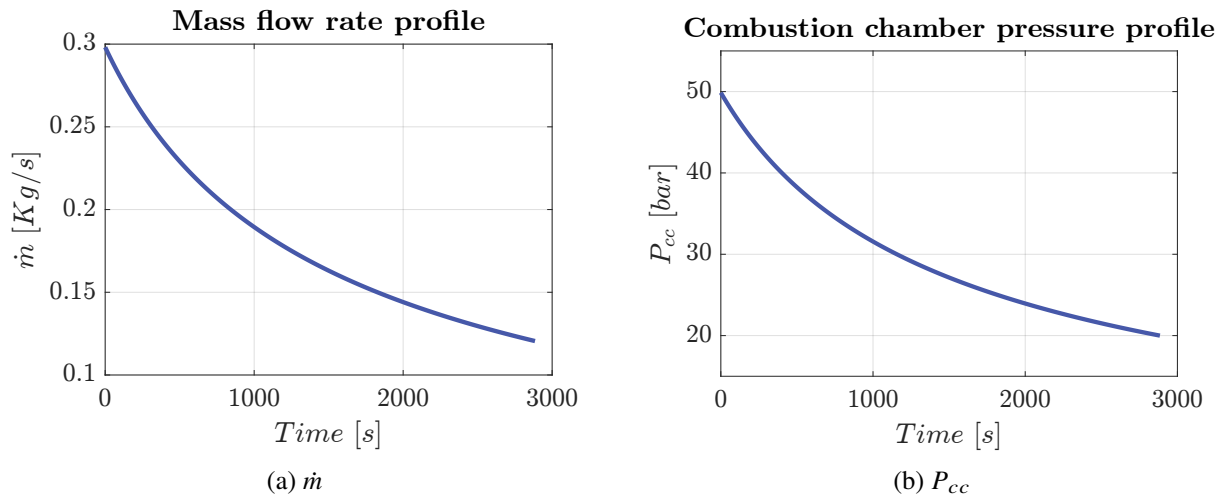


Figure 4.2.3: Mass flow rate and chamber pressure evolution

4.3 Cooling sizing results

From the procedure explained in Section 3.3, the following results are obtained:

	$T_{wh} [K]$	$q_{conv} [W/m^2]$	$T_{wc} [K]$	$q_{rad} [W/m^2]$	Err [%]
Combustion chamber	3091	6.3519e+05	2301	6.3303	0.34
Convergent nozzle	3112	9.7903e+05	2558	9.7111e+05	0.81

Table 4.9: Thermal analysis results without cooling

The values of the heat flux for both the combustion chamber and convergent nozzle satisfy the steady state hypothesis, being the relative error lower than 1%.

The wall temperatures obtained exceed the maximum operating temperature of Inconel 718 which is 977 K.^[19] The necessity of a cooling system is therefore required.

Following the operation described in Section 3.3.1 the following data are retrieved:

$\Delta T_{cc} [K]$	$\Delta T_{conv} [K]$	$T_{f_{coolant}} [K]$	$\dot{m}_{coolant} [kg/s]$
490.4	368.0	1152.6	0.0551

Table 4.10: Cooling design sizing results

The temperature reached by RP-1 is higher than the choking temperature (723 K^[45]), meaning that thermal decomposition occurs. Moreover, the second check on the mass necessary to cool down the system to reach the desired operating temperature shows that, in the burning time of the engine, the required mass is less than the stored one. The difference might be due to the approximation on the mass flow rate used for the calculation in Section 3.3.1.

4.4 Uncertainty analysis

To be able to correctly interpret the graphs resulting from the uncertainty analysis, a brief consideration about the oxidizer to fuel ratio against the temperature plot is necessary. Figure 4.4.1 shows that the O/F ratio selected for the engine design is below the stoichiometric value.

The plateau can be reached from two different sides depending on the configuration, either starting *fuel rich* or *oxidizer rich*. The fuel rich configuration is used for this engine design and characterized by a higher slope with respect to the other one. Moreover, this configuration is widely adopted due to its effectiveness.

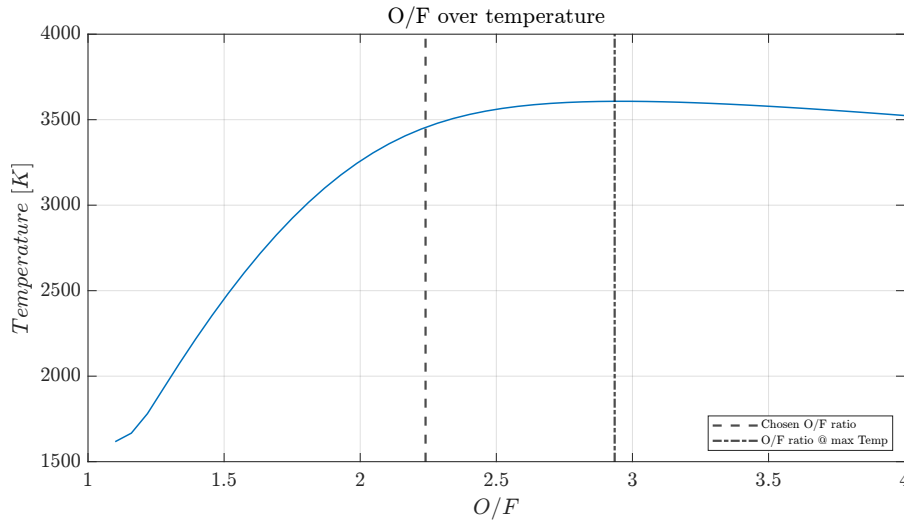


Figure 4.4.1: O/F over temperature for the nominal case

The variation of mass flow rate and O/F ratio in the 4 cases, shown in Figure 4.4.2, can be used to justify the behaviour of the other quantities.

It can be noticed that the two conditions that deviate with respect to the nominal O/F ratio are only the unbalanced combination $[D_{ox} \max D_{fuel} \min]$ and $[D_{ox} \min D_{fuel} \max]$. In the other two cases the quantities of oxidizer and fuel are counterbalanced, resulting in O/F ratio close to the nominal case. Furthermore, it is noticed that towards the end of the simulation all cases tend to converge towards the O/F ratio chosen for the sizing system. To understand the behaviour, the mass flow rate in Figure 4.4.2b has to be taken into account.

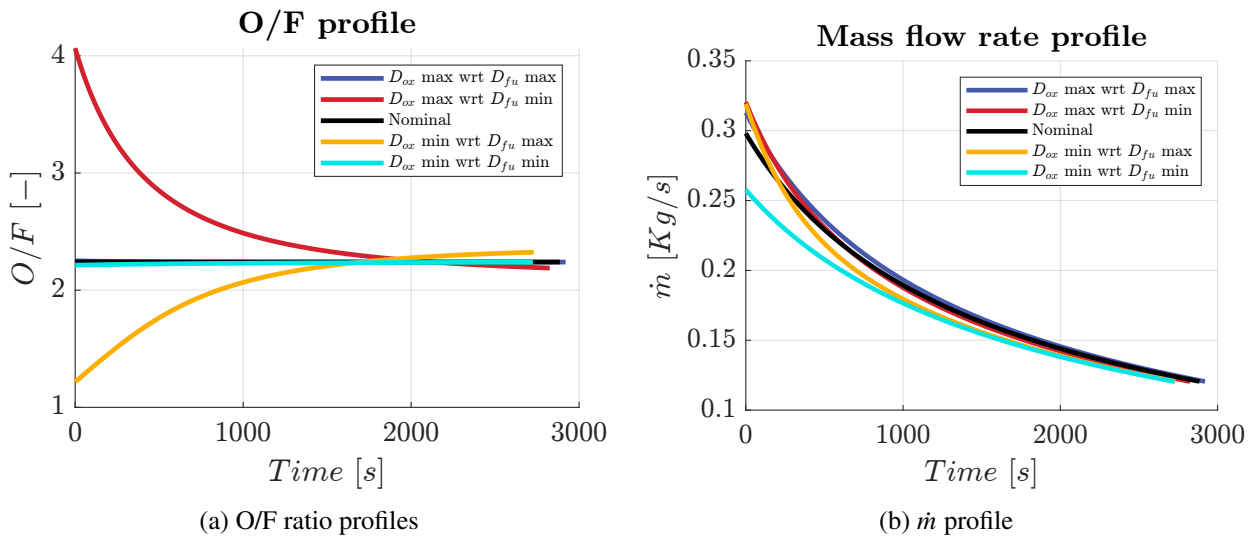


Figure 4.4.2: O/F ratio and \dot{m} evolution

In fact, in case of $[D_{ox} \max D_{fuel} \min]$, initially the system evolves consuming more oxidizer than fuel, burning with a higher O/F ratio. Thus, the mass flow rate of the oxidizer (the larger diameter) will rapidly decrease due to the fast discharge of the tank's pressure, converging towards a lower O/F ratio. For the case of $[D_{ox} \min D_{fuel} \max]$ the system starts with a lower O/F that increases because of the same principle.

This also explains the reason why, towards the end of the simulation, the $[D_{ox} \min D_{fuel} \max]$ O/F is higher than the nominal configuration: there's still a little more oxidizer in the tank to be burned, and the opposite behaviour can be seen for the $[D_{ox} \max D_{fuel} \min]$.

The I_{sp} behaviour is represented below and can be interpreted along with the previous considerations on O/F ratio and mass flow rate.

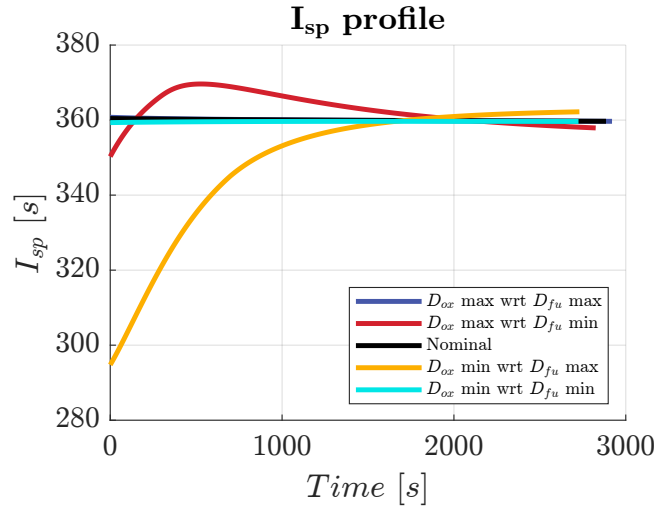


Figure 4.4.3: I_{sp} evolution

In particular, it is interesting to notice the evolution of I_{sp} in the case $[D_{ox} \max D_{fuel} \min]$, characterized by a sign change of the slope. The O/F ratio is in fact ranging from *Oxidizer rich* to *Fuel rich* (in approx. 500 seconds) passing through the "plateau" of the O/F stoichiometric. This behaviour can be justified as the optimum burning mixture is at the plateau and, by passing through it, the impulse rises and lowers.

In Figure 4.4.4 the behaviour of the combustion chamber pressure is represented. The evolution of all cases can be justified looking at the mass flow rate graph combined with O/F ratio.

- **$[D_{ox} \min D_{fuel} \min]$** : The I_{sp} contribution is at nominal condition, since O/F is nominal. At the same time, the mass flow rate is at lowest and so the P_{cc} is lower than the nominal;
- **$[D_{ox} \min D_{fuel} \max]$** : The total mass flow rate is higher, but with a lower O/F than nominal. Therefore, the P_{cc} is once again lower;
- **$[D_{ox} \max D_{fuel} \max]$** : The mass flow rate and the I_{sp} are both high. As a consequence P_{cc} is higher;
- **$[D_{ox} \max D_{fuel} \min]$** : In this case, a higher P_{cc} case was expected, since \dot{m} and I_{sp} were both higher. However, the results show a lower case than the nominal. To prove that the different behaviour of this condition was due to the fact that it is the only one starting Oxidizer rich, thus transitioning over the O/F stoichiometric, a further analysis was carried out.

The same analysis was conducted with a lower level of uncertainties, so that the case **$[D_{ox} \max D_{fuel} \min]$** started before the plateau of O/F and not after. The resulting P_{cc} was higher than the nominal, as expected, showing a better correlation with the other three results.

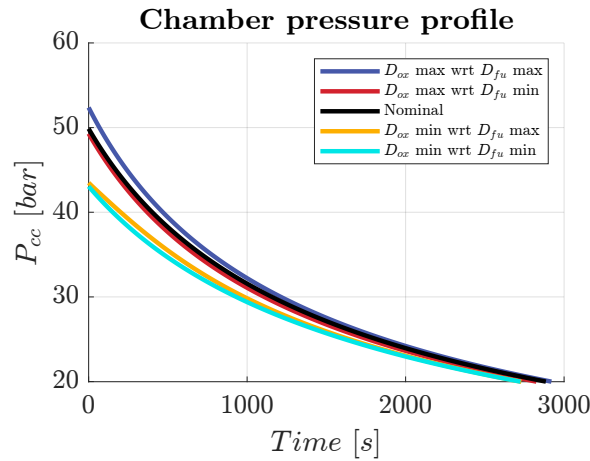


Figure 4.4.4: P_{cc} evolution

The last parameter analyzed was T_{real} , shown in Figure 4.4.5

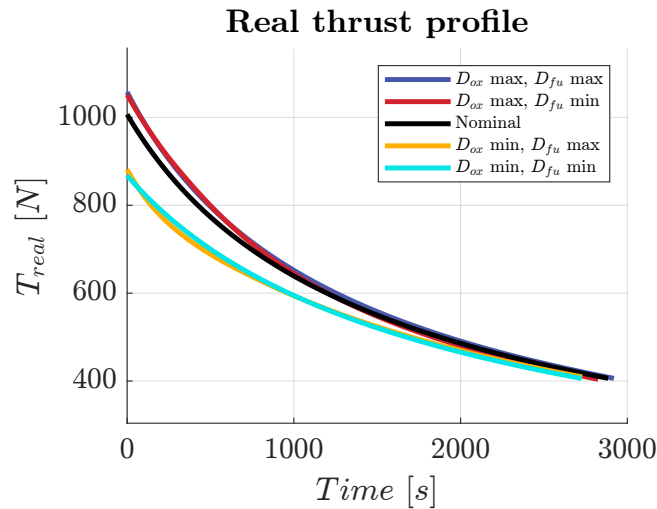


Figure 4.4.5: Thrust evolution

The thrust instead shows a clear dependency on the D_{ox} , regardless of D_{fu} . Being the thrust the product between \dot{m} and I_{sp} , through the constant value g_0 , its behaviour is justified looking at the respective profiles.

In the following table the total impulse is reported.

$Ox_{err} \backslash Fu_{err}$	D_{max}	D_{min}
D_{max}	1791.153	1732.930
D_{min}	1552.072	1552.303

Table 4.11: Total impulse [kNs] wrt diameter error

The values showed in Table 4.11 are coherent with the data shown above: the O/F ratio is preserved in the two cases where the error on the injectors' diameter is the same. For [**D_{ox} max D_{fuel} max**], the total impulse is the highest, meanwhile, for [**D_{ox} min D_{fuel} min**], the value is lower than the nominal one.

The alternative [D_{ox} **min** D_{fuel} **max**] gives a total impulse that is the lowest of the four. This is because the fuel rich combustion is unable to consume all the RP-1, making it part of the combustion product. This influences the enthalpy balance of the combustion: part of the fuel remains unburned and its high enthalpy of formation lowers the available enthalpy given by the reaction, also diminishing the temperature inside the combustion chamber.

In the remaining case [D_{ox} **max** D_{fuel} **min**], the diameter of the oxidizer is the higher one and gives a slightly lower total impulse than the nominal one. This occurs because the thrust realigns with the nominal faster than the higher case and then continues to descend remaining slightly below it, reflecting the behaviour of the mass flow rate.

5 Discussion

5.1 Further improvements

5.1.1 Injector plate

For the injection, *like on like doublet* was chosen because of its simplicity and generally attributable stable combustion and moderate performance; however, with similar orifice diameter and pressure drop, an *unlike triplet* with O-F-O arrangement could have been chosen because of better atomization performance, even though it would have imposed more constraints on the number and arrangement of holes.

5.1.2 Tanks

The assumption of cylindrical tanks was done in order to simplify the sizing, in a finer model a more realistic design should be implemented. In fact, they would have been built with spherical domes to better redistribute the strains caused by the internal pressure. However, it must also be considered that spherical domes may leave more unoccupied space in the given volume constraint.

Tanks used in real life consider different geometries like the one shown below in the Figure 5.1.1. The upper stage of *Ariane 5* used spherical (Titanium) tanks for hydrazine storage, while other designs consist in building a cylinder topped up with two half spheres as can be seen in the right figure.



(a) Ariane 5 tank^[46]



(b) Composite hydrogen tank^[47]

Figure 5.1.1: Two different types of tanks

5.1.3 Thermal analysis

Further improvements on this topic could focus on cooling methods that can be added to the already discussed ones in order to successfully maintain an adequate temperature of the combustion chamber walls. Starting from the regenerative cooling a layer of thermal coating could be added on the inside walls of the chamber^[48]. Another alternative could be the lowering of the O/F ratio in order to have a lower T_f : this allows to have a higher mass flow rate in the cooling system at the expense of the I_{sp} of the engine. With a fine tuning of the O/F ratio, it is possible to trade off the decrease in performance and the flame temperature. Another improvement could be implementing regenerative and radiative cooling in the divergent part of the nozzle, as done in the *Merlin 1D Vacuum Engine* by SpaceX.

5.1.4 Uncertainty analysis

The uncertainty analysis done in this report focuses only on the extreme cases, in order to evaluate both the higher and lower bound and the most off-nominal cases. For a better evaluation of the effect of the uncertainty given by the additive manufacturing, a stochastic analysis could be done by defining a normal curve such that

the value at 3σ is equal to the maximum error on the diameter given by both the production tolerance and the material roughness. Moreover, as the combustion chamber and the convergent part of the nozzle are also made in additive manufacturing, a Montecarlo analysis could be done by defining gaussian distributions associated with the following uncertainties:

1. injector diameters;
2. nozzle throat area;
3. friction factor of the internal walls of the combustion chamber.

Then, by performing simulations with these varying parameters, the performances can be evaluated and their coupled effects can be analysed. Furthermore, a better evaluation of the expected thrust and performances evolution can be studied by analysing the distribution of the simulation outputs with respect to the nominal values.

5.1.5 Post-machining Refinement

Although SLM is assumed to be effective to produce components that have complex geometry, post-processing including heat treatments and surface treatments is considered inevitable to obtain expected surface quality in the components. For example, finish machining (FM) and drag finishing (DF) post-processes have been shown to be able to remove up to 96 and 88% of the surface roughness in Inconel 718.^{[17][23]} A further analysis could be computed to observe the uncertainty effects after different post-machining method.

5.2 Engine applicability and feasibility

The presented engine shows several criticalities that reduce its possible applications. Firstly, the constraint of the optimal condition in vacuum and the choice on the expansion ratio of 200 leads to a in-space application.

The engine is characterized by a low thrust and this reduces the field of applicability to higher-stage or maintenance maneuver. However, the LOX is affected by low storability, caused by its tendency to evaporate and the need to be kept in cryogenic conditions. For this reason, maintenance maneuvers with LOX should be avoided; this leads to an higher-stage usage, mainly to move from a parking orbit to a interplanetary transfer or heliocentric orbit.

In addition to this, the combination of LOX and RP-1 poses additional problems, as the latter has to be kept at ambient temperature. Recent studies revolving on the feasibility of liquid engines for interplanetary mission focus on different fuel combinations, mostly LOX/CH₄ because of their similar cryogenic conditions (90K for LOX and 111K for CH₄), that avoids the need for thermal isolation between the tanks.^[49]

Moreover, the blow-down system results in a thrust that decreases with time. It may be worth it to implement throttling or regulator valves to address this issue. Furthermore, a blow-down system is usually implemented with a monopropellant fuel (mostly hydrazine), as this better exploits the simplicity granted by this type of systems with respect to regulated pressure fed ones. Moreover, this simplicity also implies lower costs; this is counter-balanced by the usage of two propellants, whose higher complexity implies higher costs both for safety and manufacturing reasons.

6 Conclusion

A preliminary design for a new product branch based on liquid semi-cryogenic propulsion (LOX-RP1) to be operated in vacuum was completed. The modeling procedure was supported by a literature analysis on blow-down architectures, nozzle losses and metallic additive manufacturing uncertainty.

The end product of the design consists in two blow-down tanks in Ti-5Al-2.5Sn, an Inconel 718 combustion chamber and injector plate, and a conical nozzle with an Inconel 718 converging section and a graphite diverging part. All Inconel 718 components were chosen to be manufactured with SLM. The material selection for the whole engine was completed with the aim to minimize the weight and maximise the performance.

The conducted thermal analysis showed that the engine cannot be cooled with RP1 during its full operative life. A possible alternative to fix this issue is to use thermal coating or implement regenerative and radiative cooling in the nozzle.

The performance analysis shows that the engine covers all the set requirements for thrust, initial and final pressures, total space allocated, blow-down architecture, and AM production. A trade-off between performance and requirements had to be considered, since both aspects were considered crucial in the design. The uncertainty given by the AM was taken into account by considering a roughness of $21\ \mu\text{m}$ and an accuracy of $\pm 0.76\ \text{mm}$. This has a significant influence on all parameters, especially when applying two opposite uncertainty values on the fuel and oxidizer diameters in the injector plate. A stochastic approach could be implemented to better represent the obtainable results.

The applicability of the designed engine was analyzed, arriving to the conclusion that it could be applied only in specific cases among upper-stages propulsion systems. Additive manufacturing can be of great use for the production of components in a liquid propulsion system; however, the current lack of accuracy and surface quality result in a level of uncertainty in the performances. Post-machining refinement are widely adopted in industry to remove these limits and have an improved control on the performances.

7 Authorship declaration

Authorship declaration	
Surname	Technical tasks
Airoidi	Literature analysis (Additive manufacturing), Feeding lines, Thermal analysis, Research for numerical values assumed, Preliminary Uncertainty Analysis.
Bachini	Injection plate design, Passive thermal analysis, Uncertainty analysis MATLAB code, Data post processing.
Belletti	Tank sizing, all bottom up MATLAB code, Nozzle sizing (performance evaluation), Preliminary uncertainty analysis, 2D and 3D modelling.
De Luca	Nozzle sizing, Combustion Chamber sizing, Thermal analysis (MATLAB codes), Research on engines to support Mach in the CC.
De Magistris	Literature analysis (Blow-down), Injection plate design, Thermal analysis, Uncertainty analysis MATLAB code, Data post processing.
De Marco	Nozzle sizing, Combustion Chamber sizing, Tank sizing, Preliminary uncertainty analysis, Selection of L^* , ε_c and ε .
Perusini	Literature analysis (Blow-down, Additive manufacturing, Injector Plate), Feeding line losses, preliminary Uncertainty Analysis.
Poverini	Literature analysis (Blow-down, Nozzle losses + computation), Material choice appendix, Feeding lines, Selection of L^* , ε_c and ε appendix, Research on engines to support Mach in the CC, Research for numerical values assumed.
Topuz	Topdown simulation and MATLAB code, Injection plate design, Tank sizing.

A Data selection

A.1 Reference tables

TABLE 5-5. Theoretical Chamber Performance of Liquid Rocket Propellant Combinations

180	Oxidizer	Fuel	Mixture Ratio		Average Specific Gravity	Chamber Temp.(K)	Chamber c^* (m/sec)	\bar{M} , (kg/mol)	I_s (sec)		
			By Mass	By Volume					Shifting	Frozen	k
Oxygen	Methane		3.20	1.19	0.81	3526	1835	20.3		296	1.20
			3.00	1.11	0.80	3526	1853		311		
		Hydrazine	0.74	0.66	1.06	3285	1871	18.3		301	1.25
			0.90	0.80	1.07	3404	1892	19.3	313		
		Hydrogen	3.40	0.21	0.26	2959	2428	8.9		386	1.26
	RP-1		4.02	0.25	0.28	2999	2432	10.0	389.5		
			2.24	1.59	1.01	3571	1774	21.9	300	285.4	1.24
			2.56	1.82	1.02	3677	1800	23.3			
		UDMH	1.39	0.96	0.96	3542	1835	19.8		295	1.25
			1.65	1.14	0.98	3594	1864	21.3	310		
Fluorine	Hydrazine		1.83	1.22	1.29	4553	2128	18.5	334		1.33
			2.30	1.54	1.31	4713	2208	19.4		365	
		Hydrogen	4.54	0.21	0.33	3080	2534	8.9		389	1.33
Nitrogen tetroxide	Hydrazine		7.60	0.35	0.45	3900	2549	11.8	410		
			1.08	0.75	1.20	3258	1765	19.5		283	1.26
			1.34	0.93	1.22	3152	1782	20.9	292		
	50% UDMH		1.62	1.01	1.18	3242	1652	21.0		278	1.24
		50% hydrazine	2.00	1.24	1.21	3372	1711	22.6	289		
		RP-1	3.4	1.05	1.23	3290		24.1		297	1.23
		MMH	2.15	1.30	1.20	3396	1747	22.3	289		
Red fuming nitric acid	RP-1		1.65	1.00	1.16	3200	1591	21.7		278	1.23
			4.1	2.12	1.35	3175	1594	24.6		258	1.22
			4.8	2.48	1.33	3230	1609	25.8	269		
		50% UDMH	1.73	1.00	1.23	2997	1682	20.6		272	1.22
Hydrogen peroxide (90%)	50% hydrazine		2.20	1.26	1.27	3172	1701	22.4	279		
		RP-1	7.0	4.01	1.29	2760		21.7		297	1.19

Figure A.1.1: Table 5-5 from Sutton book^[3]

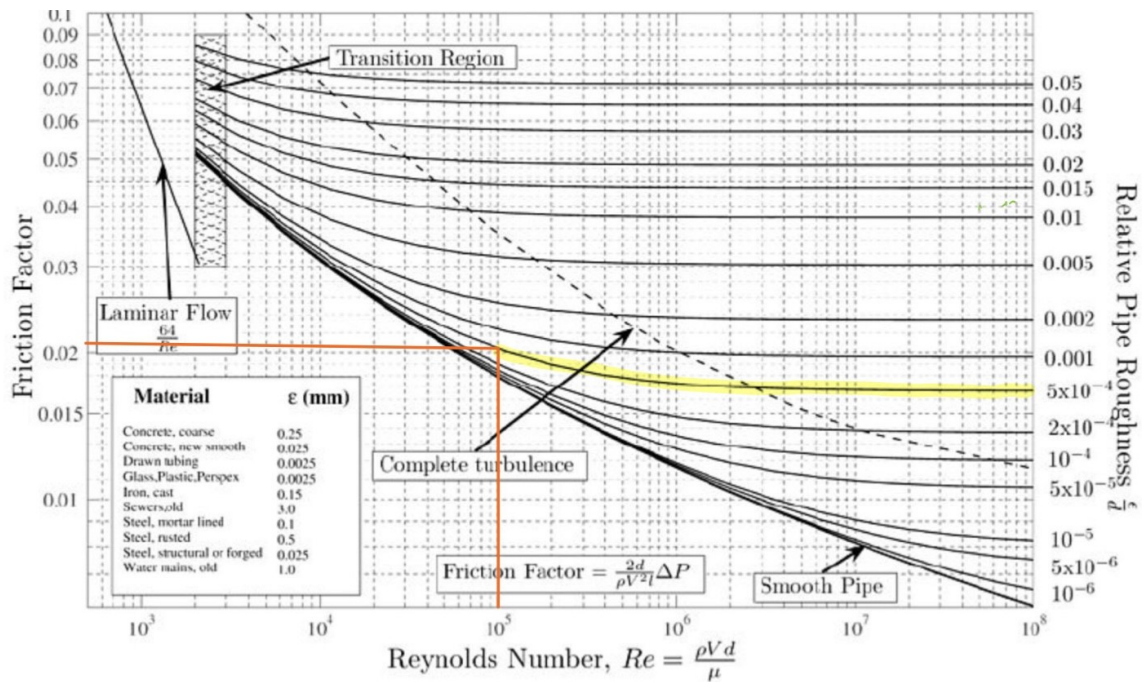


Figure A.1.2: Moody diagram^[4]

A.2 Selection of L^* , ε_r and ε_c

In order to choose the most suitable values of L^* , ε_r and ε_c , the bottom-up was carried out exploiting the possible range of the three values.

Regarding L^* , from the range 40''–50'' for the propellant couple LOX/RP-1^[50], the length of the combustion chamber was considered. Since the model of frozen expansion was adopted, the value of L^* was selected in order to have a longer combustion chamber over a shorter one, so that the residence time allowed to attain chemical equilibrium within the chamber. A characteristic length of 50'' was then selected.^[3]

Once the value of L^* was fixed, the values of ε_r was chosen as 200 in the range 100–400 to have a reasonable divergent length. ε_c was selected equal to 10 in the range 5–15 in order to have an intermediate value for both radius and length of the combustion chamber. Tables A.1 to A.3 differ in terms of the value of ε_c and show the changing of geometrical parameters due to the different selection of ε_r in its range keeping L^* equal to 50''.

ε_r [-]	L_d [m]	L_c [m]	L_{cc} [m]	r_{cc} [m]	r_t [m]
100	0.1988	0.0146	0.1058	0.0205	0.0059
200	0.2878	0.0145	0.1058	0.0203	0.0059
400	0.4131	0.0144	0.1058	0.0202	0.0058

Table A.1: ε_c equal to 12

ε_r [-]	L_d [m]	L_c [m]	L_{cc} [m]	r_{cc} [m]	r_t [m]
100	0.1988	0.0097	0.1814	0.0157	0.0059
200	0.2878	0.0097	0.1814	0.0155	0.0059
400	0.4131	0.0096	0.1814	0.0154	0.0058

Table A.2: ε_c equal to 10

ε_r [-]	L_d [m]	L_c [m]	L_{cc} [m]	r_{cc} [m]	r_t [m]
100	0.18	0.0128	0.1270	0.0187	0.0059
200	0.2878	0.07	0.1270	0.0186	0.0059
400	0.41	0.0126	0.1270	0.04	0.0058

Table A.3: ε_c equal to 7

A.3 Computation of λ and C_d

Modifying the geometry leads to changes in the values of λ and C_d . The value of λ changes depending on the type of divergent that is analyzed:

$$\lambda = \frac{1}{2} \left[1 + \cos \left(\frac{\alpha' + \theta_e}{2} \right) \right] \quad (\text{A.3.1})$$

$$\lambda = \frac{1 + \cos(\alpha)}{2} \quad (\text{A.3.2})$$

Where:

$$\alpha' = \arctan \left(\frac{r_{exit} - r_t}{L_{div-bell}} \right) \quad (\text{A.3.3})$$

$$\alpha = \arctan \left(\frac{r_{exit} - r_t}{L_{div-con}} \right) \quad (\text{A.3.4})$$

Furthermore, the C_d :

$$C_d = 1 - \left(\frac{k+1}{2} \right)^{3/4} \left(3.266 - \frac{2.128}{k+1} \right) Re'^{-1/2} + 0.9428 \left(\frac{(k-1)(k+2)}{(k+1)^{1/2}} \right) Re'^{-1} \quad (\text{A.3.5})$$

With the computation of Re' by assuming a $r_c = 0.382 \cdot r_t$, as in the Rao approach theory:

$$Re' = \sqrt{\frac{r_t}{r_c}} Re_t \quad (\text{A.3.6})$$

B Materials selection and chemical compatibility

Materials chemical compatibility is shown in Table B.1 where "C" means Compatible, "NA" means Not Available and "NR" means Not Recommended. To verify the compatibility between RP-1 and the selected materials, sources indicating compatibility between materials and Kerosene were sought, as RP-1 is a type of Kerosene used as liquid fuel.

Substances	Titanium	Stainless Steel	Inconel	Graphite
He	C ^[51]	C ^[44,52]	C ^[44]	C ^[53]
LOX	NR ^[54]	C ^[44]	C ^[44]	C ^[53,55]
RP-1	NA ^[44,56]	C ^[44,52]	C ^[44]	C ^[53,55]

Table B.1: Materials chemical compatibility

B.1 Tanks

In order to select the appropriate tank material, consideration was given to chemical compatibility, weight and mechanical properties. Given the requirement for cryogenic storage of the oxidizer (LOX), titanium alloy Ti-5Al-2.5Sn was selected due to its compatibility with cryogenic applications, its density, which is approximately half that of steels and its excellent yield and fracture strength, as well as its corrosion resistance^[54,57]. The issue with this alloy is its high reactivity with oxygen, which is why it cannot be used in launch vehicles^[54,58,59]. One potential solution involves physically separating LOX from the titanium alloy using a non-reactive material such as SS304L, which is known to be chemically compatible with LOX (As shown in Table B.1). Since both titanium alloy and stainless steel are compatible with cryogenic applications, the final decision is to use an RP-1 tank entirely made of Ti-5Al-2.5Sn, while the LOX tank will consist of a bilaminate composite made of Ti-5Al-2.5Sn with a thin internal film of SS304L to separate it from liquid oxygen.

B.2 Injection plate and combustion chamber

Inconel 718 is a well-known work material that has been widely used in various industries due to its properties such as its excellent creep performance, high yield and tensile strength. This material is selected for the injection plate and the combustion chamber because it is suitable for additive manufacturing^[22,23] and chemically compatible with the propellants and the pressurizer (See Table B.1). This methodology is considered as effective in fabricating components with complex geometries; post-processing procedures, such as heat treatments and surface treatments, play a crucial role in regulating and enhancing the microstructural characteristics of additively manufactured parts.

B.3 Nozzle

The nozzle is made of two different materials, one for the convergent section and one for the divergent section. The convergent section is constructed using additive manufacturing, hence made of Inconel 718, whilst the divergent section is made of graphite. Graphite is a widely used component in rocket nozzles due to its many advantageous properties. It was chosen as the material for the nozzle divergent due to its high temperature resistance, good thermal conductivity and low cost^[60,61].

B.4 Final selection

The final materials selection is shown in Table B.2

Tanks	Injection plate	Combustion chamber	Nozzle convergent	Nozzle divergent
Ti-5Al-2.5Sn + SS304L	Inconel 718	Inconel 718	Inconel 718	Graphite

Table B.2: Final materials selection

C Dittus-Boelter

The following thermal analysis implements the Dittus-Boelter model, even if the validity ranges of the Pr and the $\frac{L}{D}$ are not respected.

$$Nu = \frac{h d_c}{k_{gas}} = C \cdot Re_{Dh}^{0.8} Pr^n \quad \left\{ \begin{array}{l} 0.7 \leq Pr \leq 160 \\ 10000 \leq Re_{Dh} \\ L_{cc}/D_{cc} \geq 10 \end{array} \right. \quad (C.0.1)$$

The values of C and n are chosen to be, respectively, 0.0265 and 0.3 as the fluid is cooling. The Reynolds number was computed by using as characteristic length the hydraulic diameters of the combustion chamber and throat.

Combustion chamber				Throat			
$L_{cc}/D_{cc}[-]$	$Re_{dc}[-]$	$Pr[-]$	$h[W/m^2K]$	$L_{div-con}/D_t[-]$	$Re_{dc}[-]$	$Pr[-]$	$h[[W/m^2K]$
3.42	6.77e+04	0.620	568.9	1.08	2.2322e+05	0.625	3.98e+03

Table C.1: Values for thermal analysis from Dittus-Boelter model

	$T_{wh}[K]$	$q_{conv}[W/m^2]$	$T_{wc}[K]$	$q_{rad}[W/m^2]$	$Err [\%]$
Combustion chamber	2894	3.8516e+05	2029	3.8275e+05	0.63
Convergent nozzle	2993	7.7692e+05	2418	7.7610e+05	0.11

Table C.2: Thermal analysis results without cooling from Dittus-Boelter model

$\Delta T_{cc}[K]$	$\Delta T_{conv}[K]$	$T_{f,coolant}[K]$	$m_{coolant}[kg]$
210.8	114.2	619.2	164

Table C.3: Cooling design sizing results from Dittus-Boelter model

Comparing the results with the ones obtained from the Gnielinski model (Section 4.3), according to the analysis with Dittus-Boelter, the coolant does not reach the coking temperature. The reason of the discrepancies between the models can be justified by the fact that the validity ranges of Dittus-Boelter are not respected, as the model loses validity outside the given ranges.

References

- [1] W. Tillmann, C. Schaak, J. Nellesen, M. Schaper, M. Aydinöz, and K.-P. Hoyer, “Hot isostatic pressing of in718 components manufactured by selective laser melting,” *Additive Manufacturing*, vol. 13, pp. 93–102, 2017. [Online]. Available: <https://www.sciencedirect.com/science/article/pii/S2214860416300495>
- [2] J. Hulka, R. Osborne, “Additive manufacturing of liquid rocket engine combustion devices: A summary of process developments and hot-fire testing results,” 2018.
- [3] G.P. Sutton, O. Biblarz, *Rocket Propulsion Elements*, 9th ed. Wyler, 2016.
- [4] R.D. Zucker, O. Biblarz, *Fundamentals of gas dynamics*, 2nd ed. John Wiley & Sons, 2019.
- [5] H. Rocketry, “Pressure fed rockets - regulated vs. blowdown.”
- [6] E. Schmidt, G. Brewster, and G. Cain, “Mars lander retro propulsion,” in *Paper IAF-99-S.2.02*, 10 1999.
- [7] M. Ellion and D. Frizell, R. Meese, *Liquid propulsion systems for orbit insertion of unmanned spacecraft*. AIAA, 2012. [Online]. Available: <https://arc.aiaa.org/doi/abs/10.2514/6.1976-711>
- [8] C. Alessandro, “Nozzle theory lecture notes,” Sapienza Università di Roma.
- [9] “Rocket nozzles,” Purdue University. [Online]. Available: <https://www.coursesidekick.com/aerospace-engineering/3470678>
- [10] J. Östlund, “Flow processes in rocket engine nozzles with focus on flow separation and side-loads,” Kungliga Tekniska Högskolan, 2002.
- [11] S. P. Tang and J. B. Fenn, “Experimental determination of the discharge coefficients for critical flow through an axisymmetric nozzle,” *AIAA Journal*, vol. 16, no. 1, pp. 41–46, 1978. [Online]. Available: <https://doi.org/10.2514/3.60854>
- [12] A. Vafadar, F. Guzzomi, A. Rassau, K. Hayward, “Advances in metal additive manufacturing: A review of common processes, industrial applications, and current challenges,” *Applied Sciences*, vol. 11, p. 1213, 01 2021.
- [13] Paul Gradl, NASA Marshall Space Flight Center, “Metal additive manufacturing for aerospace applications,” 2022.
- [14] “Iso/atm 52900:2021 additive manufacturing - general principles terminology,” 2021.
- [15] M. K. Thompson, G. Moroni, T. Vaneker, G. Fadel, R. I. Campbell, I. Gibson, A. Bernard, J. Schulz, P. Graf, B. Ahuja, and F. Martina, “Design for additive manufacturing: Trends, opportunities, considerations, and constraints,” *CIRP Annals*, vol. 65, no. 2, pp. 737–760, 2016. [Online]. Available: <https://www.sciencedirect.com/science/article/pii/S0007850616301913>
- [16] B. Blakey-Milner, P. Gradl, G. Snedden, M. Brooks, J. Pitot, E. Lopez, M. Leary, F. Berto, and A. du Plessis, “Metal additive manufacturing in aerospace: A review,” *Materials & Design*, vol. 209, p. 110008, 2021. [Online]. Available: <https://www.sciencedirect.com/science/article/pii/S0264127521005633>
- [17] Y. Kaynak and E. Tascioglu, “Finish machining-induced surface roughness, microhardness and xrd analysis of selective laser melted inconel 718 alloy,” *Procedia CIRP*, vol. 71, pp. 500–504, 2018, 4th CIRP Conference on Surface Integrity (CSI 2018). [Online]. Available: <https://www.sciencedirect.com/science/article/pii/S2212827118306413>
- [18] P. Keller, R. Mendricky, “Parameters influencing the precision of slm production,” *MM science Journal*, 2015. [Online]. Available: <https://www.mmscience.eu/journal/issues/october-2015/articles/parameters-influencing-the-precision-of-slm-production>

- [19] S. Metals, "Inconel alloy 718 properties." [Online]. Available: <https://www.specialmetals.com/documents/technical-bulletins/inconel/inconel-alloy-718.pdf>
- [20] M.D. Sangid, T.A. Book, D. Naragani, J. Rotella, P. Ravi, A. Finch, P. Kenesei, J.-S. Park, H. Sharma, J. Almer, X. Xiao, "Role of heat treatment and build orientation in the microstructure sensitive deformation characteristics of in718 produced via slm additive manufacturing," *Additive Manufacturing*, vol. 22, pp. 479–496, 2018. [Online]. Available: <https://www.sciencedirect.com/science/article/pii/S2214860418300472>
- [21] H. Fayazfar, J. Sharifi, M.K. Keshavarz, M. Ansari, "An overview of surface roughness enhancement of additively manufactured metal parts: a path towards removing the post-print bottleneck for complex geometries," *The International Journal of Advanced Manufacturing Technology*, vol. 125, no. 3, pp. 1061–1113, Mar 2023. [Online]. Available: <https://doi.org/10.1007/s00170-023-10814-6>
- [22] Y. Kaynak, E. Tascioglu, "Post-processing effects on the surface characteristics of inconel 718 alloy fabricated by selective laser melting additive manufacturing," *Prog Addit Manuf*, vol. 5, p. 221–234, 2020. [Online]. Available: <https://link.springer.com/article/10.1007/s40964-019-00099-1>
- [23] P. Gradl, O. Mireles, N. Andrew, "Intro to additive manufacturing for propulsion systems," 2018.
- [24] J. Ilčík, D. Koutný, and D. Paloušek, "Geometrical accuracy of the metal parts produced by selective laser melting: Initial tests," pp. 573–582, 2014.
- [25] N.D. Dejene, H.G. Lemu, "Current status and challenges of powder bed fusion-based metal additive manufacturing: Literature review," *Metals*, vol. 13, no. 2, 2023. [Online]. Available: <https://www.mdpi.com/2075-4701/13/2/424>
- [26] D.K. Huzel, D.H. Huang, *Modern Engineering for Design of Liquid-Propellant Rocket Engines - AIAA (1992)*. AIAA, 1992.
- [27] T. Ghidini and M. Bugatti, "Additive manufacturing for space and aerospace applications," 2024.
- [28] [Online]. Available: <https://www.mks.com/n/vacuum-basics>
- [29] Y.A. Çengel, J.A. Cimbala, *Meccanica dei fluidi*. McGraw-Hill, 2015.
- [30] V. E. Hosseini, "A review of mechanical properties of additively manufactured inconel 718."
- [31] J.C. Oefelein, V. Yang, "Comprehensive review of liquid-propellant combustion instabilities in f-1 engines," *Journal of Propulsion and Power*, vol. 9, no. 5, pp. 657–677, 1993. [Online]. Available: <https://doi.org/10.2514/3.23674>
- [32] A. Etters, M. Rober, D. Lee, C. Guernsey, M. Long, and M. Knopp, "Mars science laboratory descent stage propulsion tubing configuration and design," in *2009 IEEE Aerospace conference*, 2009, pp. 1–10.
- [33] *Low pressure gas filter datasheet*, Vacco. [Online]. Available: https://www.vacco.com/images/uploads/pdfs/filters_low_pressure.pdf
- [34] *Low pressure latch valve datasheet*, Vacco. [Online]. Available: <https://www.vacco.com/images/uploads/pdfs/V1E10454-01.pdf>
- [35] *Titanium Ti-5Al-2.5Sn datasheet*, Special Metals. [Online]. Available: <https://asm.matweb.com/search/SpecificMaterial.asp?bassnum=MTA520>
- [36] "Concurrent design facility studies standard margin philosophy description," ESA.
- [37] "Nist chemistry webbook," NIST. [Online]. Available: <https://webbook.nist.gov/chemistry/>

- [38] F.P. Incropera, D.P. DeWitt, T.L. Bergman, A.S. Lavine, *Fundamentals of Heat and Mass Transfer*. John Wiley & Sons, 2011, 1996.
- [39] "Space physics: Heat, temperature, and the electromagnetic spectrum," https://cosmicopia.gsfc.nasa.gov/qa_sp_ht.html.
- [40] B. P. Keller, S. E. Nelson, K. L. Walton, T. K. Ghosh, R. V. Thompson, and S. K. Loyalka, "Total hemispherical emissivity of inconel 718," *Nuclear Engineering and Design*, vol. 287, pp. 11–18, 2015. [Online]. Available: <https://www.sciencedirect.com/science/article/pii/S0029549315001004>
- [41] "Ignition characterization of the gox/ethanol propellant combination," NASA. [Online]. Available: <https://arc.aiaa.org/doi/10.2514/6.1984-1467>
- [42] E. Andersson, "Preliminary design of a small-scale liquid-propellant rocket engine testing platform," Luleå University of Technology. [Online]. Available: <https://www.diva-portal.org/smash/get/diva2:1375729/FULLTEXT01.pdf>
- [43] N.M.F.B. Muhalim, S. Krishnan, "Design of nitrogen-tetroxide/ monomethylhydrazine thruster for upper stage application," Universiti Teknologi Malaysia. [Online]. Available: <https://propulsion-skrishnan.com/pdf/N2O4-MMH%20Upper%20Stage%20Thruster.pdf>
- [44] "Metallic materials used in bal seal products," BALSEAL engineering. [Online]. Available: <https://pdf4pro.com/amp/view/chemical-compatibility-chart-metallic-materials-used-4ade11.html>
- [45] T. J. Bruno, "The properties of rp-1 and rp-2 - mipr f1sbaa8022g001." [Online]. Available: <https://kinetics.nist.gov/RealFuels/maccr/maccr2008/Bruno2.pdf>
- [46] "Ariane 5 fuel tank," ESA. [Online]. Available: https://www.esa.int/ESA_Multimedia/Images/2011/02/Ariane_5_fuel_tank
- [47] "Building a big rocket fuel tank," NASA. [Online]. Available: <https://www.nasa.gov/image-article/building-big-rocket-fuel-tank/>
- [48] Jorge Bertoldo Junior, Carlos de Moura Neto, Giuliano Gardolinski Venson, Daniel Soares de Almeida, "Thermal barrier coating for liquid rocket engine thrust chamber," 2010.
- [49] Mark D. Klem, "Lox/methane in-space propulsion systems technology status and gaps," NASA GRC. [Online]. Available: <https://ntrs.nasa.gov/api/citations/20170005557/downloads/20170005557.pdf>
- [50] D.K. Huzel, D.H. Huang, *Modern Engineering for design of liquid-propellant rocket engines*. American Institute of Aeronautics and Astronautics, 1992.
- [51] "Assessment of titanium alloys for fusion reactor first-wall and blanket applications." [Online]. Available: <https://www.osti.gov/servlets/purl/5171710#:~:text=The%20corrosion%20rates%20found%20in,temperatures%20below%20500%C2%B0C>.
- [52] GRACO. [Online]. Available: https://www.graco.com/content/dam/graco/ipd/literature/misc/chemical-compatibility-guide/Graco_ChemCompGuideEN-B.pdf
- [53] [Online]. Available: <https://www.parrinst.com/wp-content/uploads/downloads/2016/12/Grafoil-Gaskets-Chemical-Compatibility.pdf>
- [54] K.E. Meiners, "Mechanical properties and lox compatibility of stainless steel-clad titanium prepared by explosive welding and vacuum deposition," NASA, 1969.
- [55] [Online]. Available: <https://ddenginc.com/gaskets/spiral-wound-gaskets/graphite-filler-compatibility-chart>

- [56] [Online]. Available: <https://tricormetals.com/corrosion-chart/>
- [57] [Online]. Available: <https://www.tag.it/leghe-di-titanio-introduzione-caratteristiche-applicazioni/>
- [58] W.A. Riehl, C.F. Key, J.B. Gayle, "Reactivity of titanium with oxygen," NASA, 1963.
- [59] J.D. Jackson, W.K. Boyd, P.D. Miller, "Reactivity of metals with liquid and gaseous oxygen," DTIC, 1963.
- [60] B. Nigar, S. Dönmez, D. Çöker, and S. Özerinç, "Understanding mechanical failure of graphite rocket nozzle throats under thermal stresses," *Aerospace Science and Technology*, vol. 119, p. 107152, 2021.
[Online]. Available: <https://www.sciencedirect.com/science/article/pii/S1270963821006623>
- [61] [Online]. Available: <https://astforgetech.com/rocket-nozzles-types-manufacturing-materials/>